

DUST ATTENUATION, BULGE FORMATION AND INSIDE-OUT CESSATION OF STAR-FORMATION IN STAR-FORMING MAIN SEQUENCE GALAXIES AT $z \sim 2$ [†]

S. TACCHELLA¹, C. M. CAROLLO¹, N. M. FÖRSTER SCHREIBER², A. RENZINI^{3,4}, A. DEKEL⁵, R. GENZEL^{2,6,7}, P. LANG²,
 S. J. LILLY¹, C. MANCINI³, M. ONODERA^{8,9}, L. J. TACCONI², S. WUYTS¹⁰, G. ZAMORANI¹¹

DRAFT VERSION: April 5, 2017

ABSTRACT

We derive two-dimensional dust attenuation maps at ~ 1 kpc resolution from the UV continuum for 10 galaxies on the $z \sim 2$ Star-Forming Main Sequence (SFMS). Comparison with IR data shows that 9 out of 10 galaxies have no further obscuration in addition to the UV-based correction. The individual rest-frame V -band dust attenuation (A_V) radial profiles scatter around an average profile that gently decreases from ~ 1.8 mag in the center down to ~ 0.6 mag at $\sim 3 - 4$ half-mass radii. We use these A_V maps to correct UV- and H α -based star-formation rates (SFRs), which agree with each other. At masses $\lesssim 10^{11} M_\odot$, the specific SFR (sSFR) profiles are on average radially constant at a mass-doubling timescale of ~ 300 Myr, pointing at a synchronous growth of bulge and disk components in such galaxies. At masses $\gtrsim 10^{11} M_\odot$, the dust-corrected sSFR profiles are typically centrally-suppressed by a factor of ~ 10 relative to the galaxy outskirts. With total central obscuration disfavored, this indicates that at least a fraction of massive $z \sim 2$ SFMS galaxies have started inside-out their star-formation quenching that will move them to the quenched sequence; this also highlights the key role of progenitor bias effects in the observed evolution of the quenched population. Galaxies above and below the ridge of the SFMS relation have respectively centrally-enhanced and centrally-suppressed sSFRs relative to their outskirts, supporting a picture where bulges are built due to gas ‘compaction’ that leads to a high central SFR as galaxies move towards the upper envelope of SFMS.

Keywords: galaxies: evolution — galaxies: high-redshift — galaxies: fundamental parameters — ISM: dust, extinction

1. INTRODUCTION

The existence at any epoch of an almost linear correlation between star-formation rate (SFR) and stellar mass (M_\star), i.e. the Star-Forming Main Sequence (SFMS; Brinchmann et al. 2004; Daddi et al. 2007; Noeske et al. 2007; Salim et al. 2007; Rodighiero et al. 2011; Whitaker et al. 2012, 2014; Speagle et al. 2014; Rodighiero et al. 2014; Schreiber et al. 2015), suggests that galaxies grow in mass and size with cosmic time in a state of self-regulated semi-equilibrium (e.g., Daddi et al. 2010; Bouché et al. 2010; Genzel et al. 2010; Tacconi et al. 2010; Davé et al. 2012; Lilly et al. 2013; Dekel et al. 2013; Dayal et al. 2013; Feldmann 2015; Tacchella et al. 2016b). Understanding the details of this equilibrium, as well as the processes that permanently move galaxies out of the SFMS onto the ‘quenched’ population, necessitates spatially-resolved information within individual galaxies of their stellar mass and SFR density distributions. This is particularly important at redshifts of order $z \sim 2$, the epoch of the peak of the cosmic SFR density and of the assembly of a large fraction of the stellar mass that is seen locked in the $z = 0$ massive spheroidal population.

Our SINS/zC-SINF program of Very Large Telescope (VLT) adaptive optics (AO) SINFONI integral-field spectroscopy and Hubble Space Telescope (*HST*) imaging has returned a wealth of facts on galaxies on the $z \sim 2$ SFMS (see Section 2.1 for details and references). Specifically, in Tacchella et al. (2015a) we constrained the M_\star and SFR distributions resolved on ~ 1 kpc scales in

Electronic address: sandro.tacchella@phys.ethz.ch

¹ Department of Physics, Institute for Astronomy, ETH Zurich, CH-8093 Zurich, Switzerland

² Max-Planck-Institut für extraterrestrische Physik (MPE), Giessenbachstr. 1, D-85748 Garching, Germany

³ INAF Osservatorio Astronomico di Padova, vicolo dell'Osservatorio 5, I-35122 Padova, Italy

⁴ Department of Physics and Astronomy Galileo Galilei, Università degli Studi di Padova, via Marzolo 8, I-35131 Padova, Italy

⁵ Center for Astrophysics and Planetary Science, Racah Institute of Physics, The Hebrew University, Jerusalem 91904, Israel

⁶ Department of Astronomy, Campbell Hall, University of California, Berkeley, CA 94720, USA

⁷ Department of Physics, Le Conte Hall, University of California, Berkeley, CA 94720, USA

⁸ Subaru Telescope, National Astronomical Observatory of Japan, National Institutes of Natural Sciences (NINS), 650 North A'ohoku Place, Hilo, HI 96720, USA

⁹ Graduate University for Advanced Studies, 2-21-1 Osawa, Mitaka, Tokyo, Japan

¹⁰ Department of Physics, University of Bath, Claverton Down, Bath, BA2 7AY, UK

¹¹ INAF Osservatorio Astronomico di Bologna, Via Ranzani 1, I-40127 Bologna, Italy

[†] Based on observations made with the NASA/ESA Hubble Space Telescope, obtained at the Space Telescope Science Institute, which is operated by the Association of Universities for Research in Astronomy, Inc., under NASA contract NAS 5-26555 (programs GO9822, GO10092, GO10924, GO11694, GO12578, GO12060, GO12061, GO12062, GO12063, GO12064, GO12440, GO12442, GO12443, GO12444, GO12445, GO13669), and at the Very Large Telescope of the European Southern Observatory, Paranal, Chile (ESO Programme IDs 075.A-0466, 076.A-0527, 079.A-0341, 080.A-0330, 080.A-0339, 080.A-0635, 081.A-0672, 183.A-0781, 087.A-0081, 088.A-0202, 088.A-0209, 091.A-0126).

~ 30 such galaxies with stellar masses above $\sim 10^{10} M_{\odot}$. We found that, at the lower mass end of our sample, $M_{\star} \lesssim 10^{11} M_{\odot}$, galaxies have flat sSFR profiles on average, indicating that they are doubling their mass at all radii with the same pace. In contrast, at masses of $M_{\star} \sim 10^{11} M_{\odot}$ and slightly above, the sSFR profiles decrease towards the galaxy centers to values of $\text{sSFR}^{-1} \gtrsim t_{\text{H}}$ (with t_{H} the Hubble time), suggesting that these galaxies have started their descent towards the quenched population by decreasing their star-formation activity in their centers (i.e. quenching ‘inside-out’). In addition, the central mass density in such massive star-forming galaxies appears to have already reached the high values that characterize the $z = 0$ quenched spheroidal population of similar mass, consistent with results by [van Dokkum et al. \(2010\)](#), [Saracco et al. \(2012\)](#) and [van Dokkum et al. \(2014\)](#).

These results carry implications for both spheroid formation and quenching mechanisms at those early epochs. [Genzel et al. \(2014b\)](#) measured large nuclear Toomre Q -values in the same massive galaxies, which they interpreted as indicating that suppression of giant clump formation is responsible for the centrally-suppressed SFRs in such gas-rich high- z disks. More generally, the presence of spheroid-like stellar densities in massive SFMS galaxies with quasi-quenched cores argues for a direct link between SFMS progenitors and quenched descendant, and in turn for a continuous feeding of the quenched population with galaxies whose sizes increase with cosmic time following the same scaling of the star-forming population. This ‘progenitor bias’ effect has indeed been argued in some works to be the driver of most of the observed growth of the average size of the quenched population at masses of order $\sim 10^{11} M_{\odot}$ ([Valentinuzzi et al. 2010](#); [Saracco et al. 2011](#); [Carollo et al. 2013](#); [Cassata et al. 2013](#); [Poggianti et al. 2013](#); [Fagioli et al. 2016](#); [Williams et al. 2016](#)), i.e. the SFR- and epoch-independent characteristic mass of the galaxy mass function since at least $z \sim 4$ (e.g., [Ilbert et al. 2013](#); [Muzzin et al. 2014](#)), which at any epoch entails the bulk of the spheroidal population. Only a small, $\sim 15\%$ of the $z = 0$ spheroid population reaches masses substantially above this characteristic mass; the structural and kinematic properties of such ultra-massive and rare spheroids show unequivocal evidence for a dissipationless formation history ([Bender et al. 1989](#); [Carollo et al. 1993](#); [Faber et al. 1997](#); [Binney & Tremaine 2008](#); [Cappellari 2016](#), and references therein).

Analytical and numerical calculations provide a benchmark for interpreting the observed mass and sSFR profiles. [Lilly & Carollo \(2016\)](#) show that a mass-dependent quenching mechanism as in, e.g., [Peng et al. \(2010\)](#), acting on star-forming disks whose sSFRs and sizes follow the cosmic evolution of these parameters, lead to a stratification of stellar density in SFMS galaxies that indeed achieves spheroidal densities at the onset of quenching (without however any causal connection between stellar density and quenching which, in the model, is entirely driven by total stellar mass). In [Tacchella et al. \(2016a\)](#) and [Tacchella et al. \(2016b\)](#) we examined the VELA cosmological zoom-in simulations of [Ceverino et al. 2014](#) (see also [Zolotov et al. 2015](#)) and found that profiles of stellar mass and SFR such as those reported in [Tacchella et al.](#)

(2015a) are realized through up and down oscillation cycles within the upper and lower boundaries of the SFMS. The physical reason behind these oscillations is the alternate occurrence of strong inward gas flows and gas depletion through gas consumption and outflows (driven by feedback). The strong inward gas flows lead to substantial compression of the gas reservoir in the galaxy centers (a process which we refer to as ‘compaction’, see [Dekel & Burkert 2014](#); [Zolotov et al. 2015](#); [Tacchella et al. 2016a](#)). Compaction leads to strong central starbursts which push galaxies towards the upper SFMS envelope and add stellar mass to the bulge components. This compaction event is followed by gas depletion through gas consumption and outflows (driven by feedback), which pushes galaxies down towards the lower envelope of the SFMS.

An important issue remains however to establish whether the observed shapes of the sSFR profiles are affected by dust extinction. The main approach to correct for dust attenuation relies on applying a wavelength-dependent dust attenuation curve (e.g., [Seaton 1979](#); [Cardelli et al. 1989](#); [Fitzpatrick 1999](#); [Reddy et al. 2015](#)) to observational constraints such as the Balmer decrement (e.g., [Calzetti 1997](#)), the ratio of far-infrared (far-IR) to ultraviolet (UV) emission (e.g., [Buat & Xu 1996](#); [Witt & Gordon 2000](#); [Panuzzo et al. 2003](#); [Buat et al. 2005](#)), or the UV continuum slope ([Calzetti et al. 1994](#); [Meurer et al. 1999](#)).

Stacking data from the 3D-HST survey ([Brammer et al. 2012](#)), [Nelson et al. \(2016a\)](#) derived Balmer decrement maps in $z \sim 1.4$ galaxies, finding several magnitudes of dust attenuation localized within the innermost ≈ 3 kpc. Substantially shallower dust attenuation radial gradients are however reported in similar high- z galaxies by [Wuyts et al. \(2012\)](#) and [Hemmati et al. \(2015\)](#), based on a pixel-by-pixel SED modelling of photometric data.

Correction for dust attenuation is definitely one of the main sources of uncertainty when deriving SFRs in observations, due to the unknown chemical, physical and geometrical distribution properties of dust in external galaxies (e.g., [Draine 2003](#)). In our [Tacchella et al. \(2015a\)](#) analysis we corrected for dust attenuation the SFR profiles derived from AO VLT/SINFONI $\text{H}\alpha$ emission line maps; the dust attenuation parameter in $\text{H}\alpha$, $A_{\text{H}\alpha}$, was calculated from the galaxy-integrated A_{V} by assuming for the color excess $E(B - V)_{\text{star}} = 0.44 \times E(B - V)_{\text{gas}}$ as in [Calzetti et al. 2000](#).

In our previous analysis we assumed a radially constant attenuation profile and pointed out that, in order to explain as a dust attenuation effect the centrally-suppressed sSFR in our massive galaxies, it would require of order 3 – 5 mag extra attenuation in the galaxy centers relative to their outskirts. Such high values have been measured from ALMA maps in some $z \sim 2$ star-forming galaxies (SFGs; [Tadaki et al. 2015](#); [Barro et al. 2016](#); [Tadaki et al. 2017](#)), but the selection criteria of those samples (i.e. compact sizes of $\sim 1 - 2$ kpc, high IR fluxes and/or very red colors) are clearly very different from the [Tacchella et al. \(2015a\)](#) sample of, if anything, slightly bluer than average, SFMS galaxies at $z \sim 2$.

Nevertheless, radial variations in the dust attenuation parameter should be expected and may substantially affect the shape of the dust-corrected sSFR profiles; a direct check on our own data is thus required to ensure that

dust is not affecting the sSFR profiles of our galaxies, including the central SFR depletions at the high-mass end of the sample. In this paper we therefore use towards this end new Cycle 22 *HST* F438W (*B*) and F814W (*I*) imaging data (# GO13669). These trace respectively the far-ultraviolet (FUV) and near-ultraviolet (NUV) light distributions within our $z \sim 2$ galaxies, which enables us to measure maps of dust attenuation from the UV continuum slope on resolved on scales of ~ 1 kpc. We will show that the dust-corrected-UV SFRs are in good agreement with IR+UV SFRs, demonstrating that, in our sample, the rest-frame UV and $H\alpha$ SFRs are not substantially missing light from regions of very high dust obscuration. While our dust attenuation profiles steadily increase towards the centers, they do so with a relatively shallow slope which results in a significant dust attenuation of $A_V \approx 0.6$ mag out to ~ 10 kpc. Importantly, the centrally-suppressed sSFR in our massive sample cannot be explained by dust attenuation alone, and are evidence of a genuine suppression of star-formation activity in the centers of massive galaxies on the SFMS at $z \sim 2$.

The paper is organized as follows. In Section 2, we present the galaxy sample and the data. We review the methodology for deriving dust attenuation and SFR diagnostics in SFGs in Section 3 and present the resulting measurements in Section 4. In particular, in Section 4.6 we quantify the impact on the SFR density profiles of assuming different dust attenuation corrections. In Section 5 we discuss where they are sustaining the bulk of their star-formation activity and the growth in stellar mass, i.e. whether in their bulge or outskirt regions. We summarize in Section 6.

Throughout this paper, we adopt WMAP9 cosmology: $H_0 = 69.3$ km s $^{-1}$ Mpc $^{-1}$, $\Omega_{\Lambda,0} = 0.71$, and $\Omega_{m,0} = 0.29$ (Hinshaw et al. 2013). For this cosmology, $1''$ corresponds to ≈ 8.4 kpc at $z = 2.2$. All sizes and radii presented in this paper are circularized, i.e. $r = r_a \sqrt{(b/a)}$. Magnitudes are given in the AB photometric system.

2. SAMPLE AND DATA

2.1. Galaxy Sample

The ten targets of this study (Table 1, Figure 1 and 2) are drawn from our SINS/zC-SINF AO program that has yielded AO-SINFONI IFU spectroscopy of the $H\alpha$ and [N II] emission lines spatially-resolved on ~ 1 kpc scales for 35 massive SFMS galaxies at $z \sim 2$ (Genzel et al. 2014b,a; Förster Schreiber et al. 2014; Newman et al. 2014; Tacchella et al. 2015b,a). The sample is virtually unique, given the long integration times of usually > 10 h to obtain $H\alpha$ spectroscopy at 8-m AO resolution. Our 10 targets were initially taken from various spectroscopic surveys, namely, 7 targets are from the zCOSMOS-DEEP survey (Lilly et al. 2007, 2009), 2 targets are from the ‘BX/BM’ sample of Steidel et al. (2004), and 1 target is from the ‘Deep-3a’ survey (Kong et al. 2006). The specific selection criteria for the SINFONI AO observations were then the observability of the $H\alpha$ emission line and a minimum expected $H\alpha$ line flux (corresponding roughly to a minimum SFR of $\sim 10 M_\odot$ yr $^{-1}$; Förster Schreiber et al. 2009; Mancini et al. 2011).

In addition to our AO-SINFONI $H\alpha$ data, these galaxies have a wealth of ancillary ground- and space-based multi-wavelength data which give integrated stel-

lar masses, global UV+IR SFRs, and other key galactic properties. Furthermore, our Cycle 19 # GO12578 program (8 targets; Tacchella et al. 2015b) together with our NICMOS pilot study (2 targets; Förster Schreiber et al. 2011a,b) have provided rest-frame optical *HST* WFC3 F110W (*J*) and F160W (*H*) data for all targets of this study. These data have given us their rest-frame optical morphology and their 1 kpc distribution of the oldest stellar populations through mass-to-light ratio estimates from the 4000Å-break (see Tacchella et al. 2015a). Figure 1 presents the data used in this paper. In particular, *HST* images, dust attenuation maps, UV and $H\alpha$ SFR maps, stellar mass maps, and $H\alpha$ velocity maps are shown.

Table 1 lists the $H\alpha$ redshift and the main stellar properties. The spectral energy distribution (SED) modeling has been presented in Förster Schreiber et al. (2009, 2011a,b) and Mancini et al. (2011). Briefly, we adopt the best-fit results obtained with the Bruzual & Charlot (2003) code, a Chabrier (2003) initial mass function (IMF), solar metallicity¹³, the Calzetti et al. (2000) reddening law, and constant SFRs. We define the stellar mass to be the integral of the SFR. The uncertainty on the stellar mass is a factor of $\sim 2 - 3$, while on the SFRs and stellar ages it is even larger. These uncertainties mainly arise due to the basic assumption of the SED modeling, namely, the IMF and the star-formation histories (SFHs). Beside the SED-derived quantities and the UV+IR SFRs, Table 1 presents the integrated values of the 2D maps of dust attenuation and UV SFR (see Section 4 for details).

Our ten galaxies have stellar masses between $10^{10} M_\odot$ and a few times $10^{11} M_\odot$ and SFRs between $60 M_\odot$ yr $^{-1}$ to $\sim 560 M_\odot$ yr $^{-1}$. In Figure 2 we show our sample of 10 galaxies in the wider context of the general population of SFGs at the same redshifts. This in order to illustrate how representative our sample is of the global galaxy population. We use the SFGs at $z = 2.0 - 2.5$ from 3D-HST survey (Brammer et al. 2012; Skelton et al. 2014) as our reference sample. Panel (a) and (b) show that our sample probes the typical SFGs on the SFMS at $z \sim 2.2$: it lies slightly above the SFMS ridgeline with $0.14^{+0.32}_{-0.30}$. We use the SFMS ridgeline of Whitaker et al. (2014), which is based on the $z = 2.0 - 2.5$ star-forming galaxy population from the CANDELS/3D-HST survey (Brammer et al. 2012; Skelton et al. 2014). In panel (c) we compare the $(U - V)_{\text{rest}} - (U - J)_{\text{rest}}$ colors of our sample to the ones of the overall galaxy population drawn from CANDELS/3D-HST survey at $z = 2.0 - 2.5$ and with $M_\star = 10^9 - 10^{11.5} M_\odot$. Our galaxies overlap with the bulk of the SFGs in terms of $(U - V)_{\text{rest}} - (U - J)_{\text{rest}}$ colors, but they do not probe the very dusty SFGs in the upper right corner of the UVJ diagram, which may well be due to small number statistics rather than to a limitation imposed by the selection criteria. Similarly, looking at the ratio of IR and UV SFR (panel d), while our sample overlaps with global population traced by the stacking analysis of (Whitaker et al. 2014) of the CANDELS/3D-HST data, our most massive galaxies lie slightly below

¹³ We refer to $Z=0.02$ with solar metallicity throughout this paper, although more recent measurements indicate that solar metallicity is closer to $Z=0.015$ (Caffau et al. 2011).

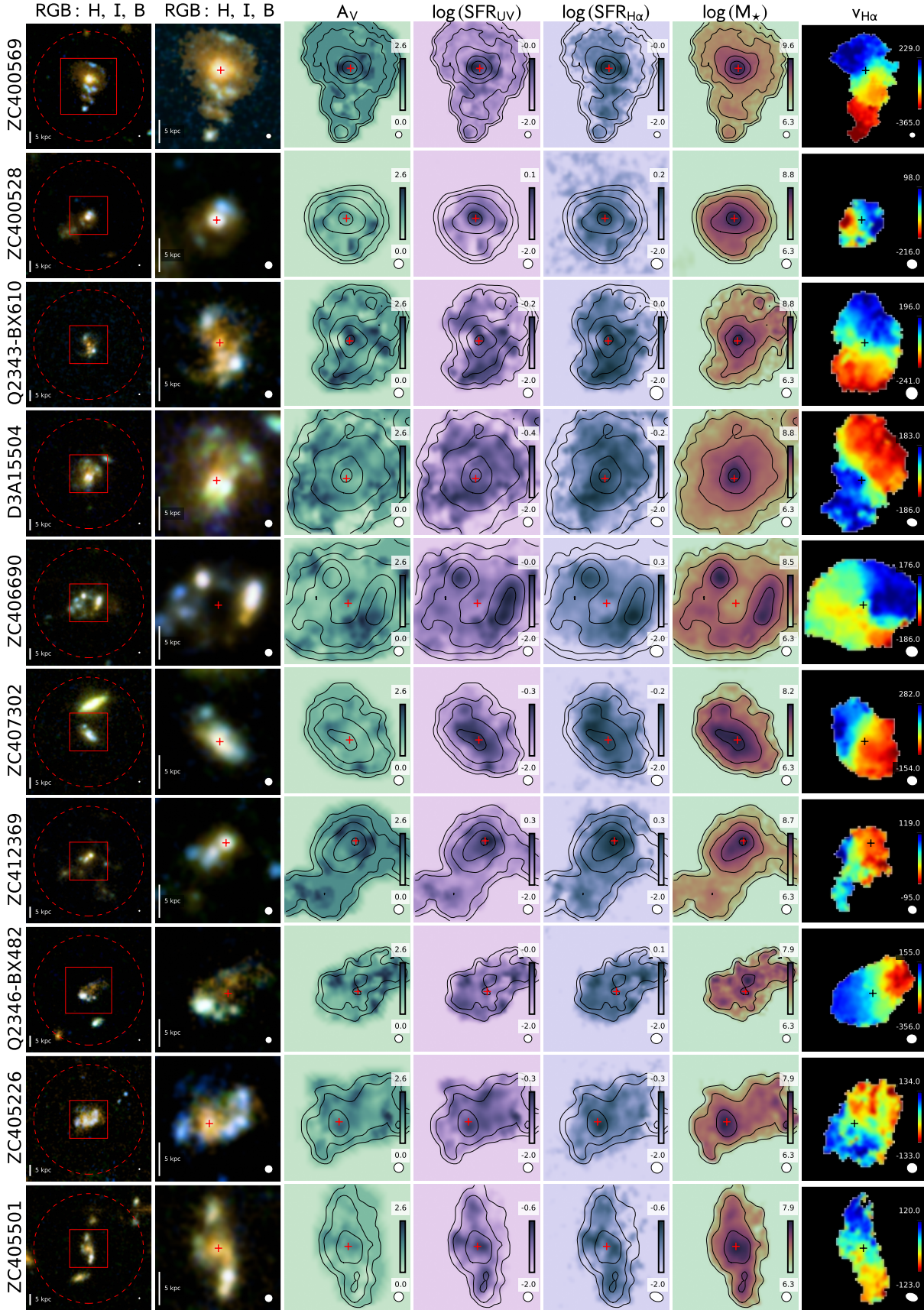


Figure 1. From left to right: *HST* RGB image (red: *H*, green: *I*, blue: *B*, all observed frame), A_V dust attenuation map (in magnitudes), dust-corrected UV SFR map (in $M_\odot \text{ yr}^{-1} \text{ kpc}^{-2}$), dust-corrected $H\alpha$ SFR map (in $M_\odot \text{ yr}^{-1} \text{ kpc}^{-2}$), stellar mass map (in $M_\odot \text{ kpc}^{-2}$), and $H\alpha$ velocity map (in km s^{-1}). Red boxes in the most left images show the field of view of the SINFONI $H\alpha$ maps and the red dashed circle indicates the $3''$ aperture of the integrated photometry. The rulers in the bottom left of the maps indicate 5 kpc and the circles in the bottom right show the size of the PSF. The contours indicate the stellar mass surface density between $\log \Sigma_M / (M_\odot \text{ kpc}^2) = 6.5$ to 9.0 in linear steps of 0.5.

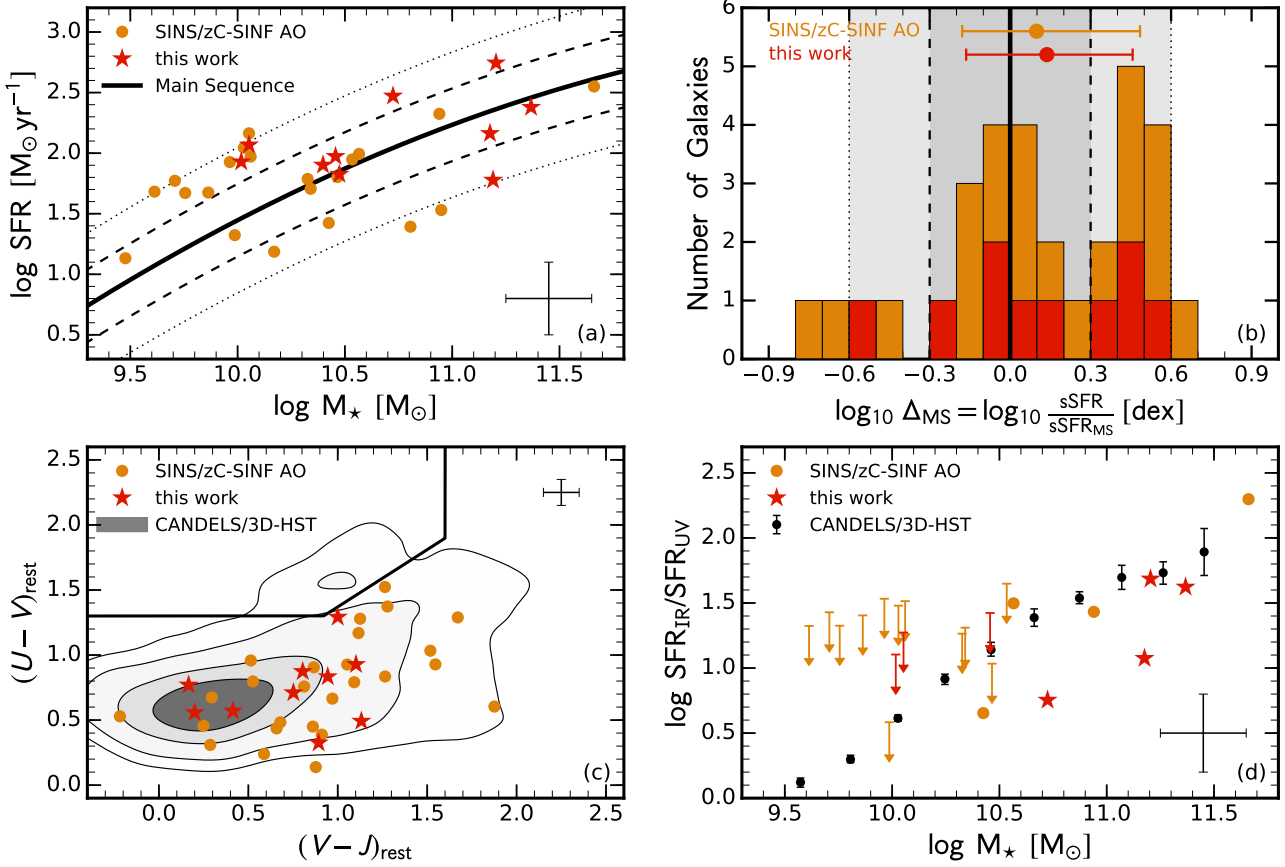


Figure 2. Our sample of galaxies relative to the global population at $z = 2.0 - 2.5$. In all panels, our sample of ten galaxies is plotted with red stars, while the parent sample SINS/zC-SINF AO is shown with orange points. *Panel (a):* The 10 galaxies of this study and the parent sample in the $\text{SFR}-M_{\star}$ plane. The quoted SFRs are UV+IR SFR (if available and reliable, otherwise SED-based SFRs). The thick solid line shows the Main Sequence ridgeline of Whitaker et al. (2014) at $z = 2.2$ (median redshift our sample), which is based on the CANDELS/3D-HST survey. The dashed and dotted lines indicate the 1σ and 2σ scatter of the Main Sequence. All 10 galaxies of our sample lies within 2σ of the Main Sequence. *Panel (b):* histogram of the distance from the Main Sequence ridgeline Δ_{MS} . Our galaxies are well distributed around the Main Sequence ridgeline. The median Δ_{MS} for our sample and the parent sample are $0.10^{+0.38}_{-0.28}$ and $0.14^{+0.32}_{-0.30}$, respectively. *Panel (c):* Our sample and the parent sample in the UVJ rest-frame color-color diagram. The gray contours show the global $z = 2.0 - 2.5$ galaxy population with $M_{\star} = 10^9 - 10^{11.5} \text{ M}_{\odot}$ drawn from the CANDELS/3D-HST survey. While our sample overlaps with global population, we do not probe the upper right region in UVJ, which may well be due to small number statistics rather than to a limitation imposed by the selection criteria. *Panel (d):* Ratio $\text{SFR}_{\text{IR}}/\text{SFR}_{\text{UV}}$ as a function of M_{\star} . Note that the UV SFR is not corrected for extinction. The black solid points show the median relation of Whitaker et al. (2014) at $z = 2.0 - 2.5$, where the IR data was stacked. Several galaxies of our sample and the parent sample are not detected in the IR (plotted are upper limits) or have no IR coverage (are not plotted). Overall, our galaxies probe the trend of the population, but only four galaxies have a reliable IR detection (see also Appendix C).

Table 1
Sample galaxies with H α redshifts and main stellar population properties.

Source	$z_{\text{H}\alpha}$	M_* [$10^{10} M_\odot$]	$(U - V)_{\text{rest}}$ [mag]	$A_{V,\text{SED}}$ [mag]	$A_{V,\text{map}}$ [mag]	SFR_{SED} [$\frac{M_\odot}{\text{yr}}$]	$\text{SFR}_{\text{UV+IR}}$ [$\frac{M_\odot}{\text{yr}}$]	Indicator	SFR_{UV} [$\frac{M_\odot}{\text{yr}}$]	$\text{SFR}_{\text{UV,map}}$ [$\frac{M_\odot}{\text{yr}}$]
ZC400569	2.241	23.3	1.29	1.4	1.5	241.0	239.3	UV+24 μm	168.0	156.6
ZC400528	2.387	16.0	0.84	0.9	0.5	148.0	556.5	UV+100 μm	148.0	46.7
Q2343-BX610	2.211	15.5	0.93	0.8	1.2	60.0	—	—	60.0	85.5
D3A15504	2.383	15.0	0.71	1.0	1.0	150.2	145.6	UV+24 μm	150.0	116.1
ZC406690	2.195	5.3	0.56	0.7	1.0	200.0	296.5	UV+24 μm	337.0	201.2
ZC407302	2.182	2.98	0.50	1.3	0.6	340.0	358.1 [†]	UV+24 μm	130.0	67.0
ZC412369	2.028	2.86	0.88	1.0	1.3	94.1	IR-undet	—	130.0	140.2
Q2346-BX482	2.257	2.5	0.77	0.8	1.1	79.8	—	—	80.0	95.8
ZC405226	2.287	1.13	0.56	1.0	0.9	117.0	IR-undet	—	87.0	58.3
ZC405501	2.154	1.04	0.33	0.9	0.6	84.9	IR-undet	—	68.0	28.1

Note. — Listed are the H α spectroscopic redshifts from the AO SINFONI data ($z_{\text{H}\alpha}$), the stellar masses (M_* ; defined as the integral of the SFR), the rest frame $U - V$ colors, the dust attenuation $A_{V,\text{SED}}$ from galaxy-integrated SED modelling, the dust attenuation $A_{V,\text{map}}$ from the (FUV – NUV) color maps, the SFRs from SED (SFR_{SED}), the UV+IR SFRs ($\text{SFR}_{\text{UV+IR}}$), the SFR indicator of the IR, SFR from the integrated UV photometry (SFR_{UV}), and the SFR from the UV maps ($\text{SFR}_{\text{UV,map}}$). For the SED modeling we use [Bruzual & Charlot \(2003\)](#) model and assume a [Chabrier \(2003\)](#) IMF, solar metallicity, the [Calzetti et al. \(2000\)](#) reddening law, and either constant or exponentially declining SFRs. The uncertainties on the stellar properties are dominated by systematics from the model assumption and are up to a factor of $\sim 2 - 3$ for M_* and ~ 3 or more for SFRs. Sources undetected with Spitzer/MIPS and Herschel/PACS are indicated explicitly with ‘IR-undet’, to distinguish them from objects in fields without MIPS and PACS observations.

[†] unreliable IR flux due to blending, see Appendix B.

the ridgeline of $\text{SFR}_{\text{IR}}/\text{SFR}_{\text{UV}}$ versus M_* of the larger sample. Finally, our sample probes the typical trends in the planes of size versus M_* and Sérsic index versus M_* , as shown and discussed in [Tacchella et al. \(2015b\)](#).

Based on [Tacchella et al. \(2015b\)](#), see also stamps in Figure 1), 9 out of our 10 galaxies are disk galaxies and only one is a clear merger. D3A-15504, Q2343-BX610, ZC405226, and ZC405501 are classified as regular disks, since at the rest-frame optical wavelengths, the galaxies show a relatively symmetric morphology featuring a single, isolated peak light distribution and no evidence for multiple luminous components. The velocity maps show clear rotation, and the dispersion maps are centrally peaked; the kinematic maps are fitted well by a disk model with $v_{\text{rot}}/\sigma_0 \gtrsim 1.5$, where v_{rot} is the inclination-corrected rotational velocity and σ_0 is the velocity dispersion corrected for instrumental broadening and beam smearing. Furthermore, Q2346-BX482, ZC400528, ZC400569, ZC406690, and ZC407302 are classified as irregular disks, because in the optical light, the galaxies have two or more distinct peaked sources of comparable magnitude. Their velocity maps show clear sign of rotation. The dispersion maps show a peak, which is, however, shifted in location relative to the centers of the velocity maps. Finally, ZC412369 is classified as a merger, since in the rest-frame optical light, two or more distinct peaked sources of comparable magnitude are detected at a projected distance ~ 5 kpc from each other. The velocity maps are highly irregular with no evidence for ordered rotation (i.e. $v_{\text{rot}}/\sigma_0 \lesssim 1.5$); the velocity dispersion maps show multiple peaks.

The AGN activity in our sample has been discussed in [Förster Schreiber et al. \(2014\)](#). None of the sources in our sample are detected in the deepest X-ray observations with Chandra ([Civano et al. 2016](#)); their flux upper limits imply $\log(L_X/\text{erg s}^{-1}) < 42.5$. For some galaxies, an AGN contribution can be argued based on the mid-IR colors (Q2343-BX610), emission lines (D3A-15504), or radio data (ZC400528).

2.2. New FUV and NUV Data

In our Cycle 22 *HST* program # GO13669, we followed up these galaxies with WFC3/UVIS and ACS/WFC observations between December 2014 and June 2015 using the F438W (*B*) and F814W (*I*) filters. Our galaxies lie in a narrow redshift range $2.03 < z < 2.39$, which puts the FUV into the *B*-band and the NUV into the *I*-band. Therefore, these two passbands cover the entire rest-frame $\sim 1200 - 2700$ Å wavelength window. This gives us the possibility to measure the UV continuum slope β in order to constrain the attenuation distribution, one of the main scientific goals of this paper. The WFC3 F438W filter is perfect for the FUV image: the cut-on wavelength of 4000 Å corresponds to 1230 – 1270 Å in the rest-frame, the long wavelength cut-off to 1450 – 1500 Å. Furthermore, the ratio of H α to rest-frame 1400 Å (probed with F438W) versus F438W-F160W will enable us to best disentangle extinction and evolutionary effects among clumps and between clumps and inter-clump regions, which will be addressed in a future publication.

Each target was observed for 4 orbits with F438W and, if necessary¹⁴, 1 orbit in F814W, with each orbit split into two exposures with a subpixel dither pattern to ensure good sampling of the PSF and minimize the impact of hot / cold bad pixels and other such artifacts (e.g., cosmic rays, satellite trails). For F438W, the individual exposure time was 1376 s, giving a total on-source integration of 11'008 s, and for F814W, the individual exposure time was 544 s, giving a total on-source integration of 2176 s.

2.3. Data Reduction

2.3.1. Charge Transfer Efficiency

The charge transfer efficiency (CTE) of the WFC3/UVIS detector has significantly degraded over time, as radiation causes permanent damage of the charge transfer device (CCD) detectors. This damage degrades the ability of electrons to transfer from one pixel to another, temporarily trapping electrons during

¹⁴ We capitalize on the existing COSMOS F814W images for the zCOSMOS targets in the current sample.

the readout. When uncorrected, the electrons are smeared out in the readout direction, appearing as trails in the images. This affects the photometry and measured morphology of the objects in the images (Massey et al. 2010; Rhodes et al. 2010). CTE degradation is most severe for low background imaging of faint sources, such as NUV imaging and calibration dark frames, where faint sources or hot pixels can be lost completely.

As mentioned before, we have one galaxy per pointing, i.e. we were able to choose freely where to place the galaxy on the CCD detector. To reduce the CTE degradation effect on our galaxies, we placed the galaxies close to the readout edge of the CCD. In addition, we apply a pixel-based CTE correction¹⁵ to the raw data based on empirical modeling of hot pixels in dark exposures (Anderson & Bedin 2010; Massey et al. 2010). This correction not only corrects the photometry, but also restores the morphology of sources.

2.3.2. WFC3/UVIS Dark Calibrations

Dark calibrations are especially important for NUV data because the dark current level in each exposure is high relative to the low sky background. In addition, regular calibration dark data can be used to identify hot pixels, which vary significantly over time. Teplitz et al. (2013) show that the darks currently provided by STScI are insufficient for data with low background levels after the CTE degradation of WFC3/UVIS. In this paper, we follow the approach of Rafelski et al. (2015) to improve the dark calibrations.

While the STScI superdarks were mostly sufficient for early data obtained soon after the installation of WFC3, subsequent changes in the characteristics of the detector (such as CTE degradation) increasingly affected the science data. There are three major areas in which the STScI processed superdarks are insufficient, namely, they fail to account for: (i) all hot pixels, (ii) background gradients, and (iii) blotchy background patterns. The dark processing methodology used in this paper is presented in detail in the Appendix of Rafelski et al. (2015).

We have used the standard procedure to convert the CTE-corrected raw data to a set of final, flat-fielded flux-calibrated images (flt-files). We used the Pyraf/STSDAS task `calwf3` to construct the bad pixel array (data quality array) and to do the bias and dark current subtraction with the new darks. In this step, we have not applied the cosmic ray rejection since we reject the cosmic rays with `drizzlepac/astrodrizzle` in a later step.

2.3.3. Astrometric Alignment

Here we discuss several sources of astrometric uncertainties in the original data, as well as our approaches to mitigating these and aligning all the images to a common reference grid. The observations were all obtained in a non-integer pixel-offset dither pattern, aimed at ensuring that the PSF was adequately sampled in the final images. Each small angle manoeuvre introduces a slight uncertainty in positioning (of the order of about 12 mas). In addition, during each orbit the spacecraft undergoes thermal expansion and contraction (‘breathing’) due to changes in solar illumination, which lead to changes in

the optical path length to the detectors, hence resulting in slight scale changes from one exposure to the next. Finally, guide star reacquisition uncertainties can lead to errors in position as well as small rotation uncertainties, while a full acquisition of a new guide star has astrometric uncertainties of $\sim 0.''3 - 0.''5$.

We make use of the source positions measured in the WFC3/F110W and F125W (*J*-band) of our previous *HST* program (# GO12578; Tacchella et al. 2015b) as our absolute astrometric reference frame. The alignment was accomplished with `drizzlepac/tweakreg` using catalog matching, which provides measurements of rotations as well as removing the bulk of the shifts that are present in the data. This technique was presented in Koekemoer et al. (2011) and already used in Tacchella et al. (2015b). The resulting overall astrometric accuracies is ~ 2 mas in the mean shift positions of all the exposures relative to one another, which is the best possible level that is achievable given the sparse number of sources and their faint flux at these wavelengths.

We use `drizzlepac/astrodrizzle` to detect cosmic rays and to dither the different exposures to one final image. We choose the same pixel scale as our previous WFC3/F110W, F125W, and F160W images, namely, of $0.05'' \text{ pixel}^{-1}$, to match the pixel scale of the SIN-FONI/AO data. This pixel scale provides an adequate sampling of the PSF. Finally, we set `pixfrac` (defines how much the input pixels are reduced in linear size before being mapped onto the output grid) to 0.8 which was found from experimentation to give the best trade-off between gain in resolution and introduction of rms noise in the final images.

2.4. Point Spread Functions (PSFs)

In order to derive PSF-matched color maps and PSF-corrected profiles as described below, PSFs of the different bandpasses are required. PSFs for each *HST* camera are created in slightly different fashions, due to varying constraints of the data.

The creation of the WFC3/NIR data PSFs is described in Tacchella et al. (2015b). Briefly, we have stacked six well exposed and non-saturated stars. The stars are registered to their subpixel centers, normalized, and then coadded via a median. The FWHM is $0.''16$ and $0.''17$ for the *J*- and *H*-band, respectively.

The ACS/WFC data and WFC3/UVIS PSFs are created with a hybrid PSF in a similar manner to the PSFs created by Rafelski et al. (2015). We follow the approach of the hybrid PSF because the wings of the PSFs cannot be recreated from a stack of stars due to the low number of stars. The PSF model is created with the TinyTim package (Krist 1995), sub-sampled to align the PSFs, re-sampled to our pixel scale, distortion corrected, and then combined with the same dither pattern and drizzle parameters as was used for the data reduction. The ACS/WFC and WFC3/UVIS stack of stars are created from four and ten unsaturated stars, respectively. The stars are registered to their subpixel centers, normalized, and then coadded via a median. The final hybrid PSF is a combination of the two, composed of the stack of stars up to a radius of 20 pixels ($0 - 1.''0$), and of the PSF model from 20 to 75 pixels ($1.''0 - 3.''75$). In order to prevent discontinuities in the resultant PSF, the PSF model and the star are added together, weighted by a

¹⁵ http://www.stsci.edu/hst/wfc3/tools/cte_tools

smooth transition window with a full width of 20 pixels (1."0). The resulting FWHM is 0."11 (2.16 pixels) and 0."11 (2.17 pixels) for the ACS/WFC F814W and WFC3/UVIS F438W, respectively.

3. METHODOLOGY FOR DERIVING DUST ATTENUATION AND SFR IN $z \sim 2$ SFMS GALAXIES

3.1. Estimating the Star-Formation Rate

3.1.1. SFR from UV

The UV continuum (1250 – 2800 Å) intensity of a galaxy is sensitive to massive stars ($\gtrsim 5 M_\odot$), making it a direct tracer of current SFR. By extrapolating the formation rate of massive stars to lower masses, for an assumed form of the initial mass function (IMF), one can estimate the total SFR.

We adopt the conversions of Kennicutt (1998), who assumed a Salpeter IMF with mass limits of 0.1 and 100 M_\odot , and stellar population models with solar metal abundance. Furthermore, they also assumed that the star formation history is constant for at least the past 100 Myr. We modify their calibration downward by a factor of 0.23 dex to match a Chabrier (2003) IMF:

$$\frac{\text{SFR}_{\text{UV}}}{M_\odot \text{ yr}^{-1}} = 0.82 \times 10^{-28} \frac{L_{\text{UV,corr}}}{\text{erg s}^{-1} \text{ Hz}^{-1}}, \quad (1)$$

where $L_{\text{UV,corr}}$ is the UV luminosity at 1500 Å corrected for attenuation, i.e. $L_{\text{UV,corr}} = L_{\text{UV,obs}} \times 10^{0.4A_{\text{UV}}}$. We derive $L_{\text{UV,obs}}$ from the observed magnitude as follows:

$$L_{\text{UV,obs}} = \frac{4\pi D_L^2(z) 10^{-0.4(48.6+m_{\text{UV}})}}{1+z}, \quad (2)$$

where $D_L(z)$ is the luminosity distance at z , and m_{UV} is the observed magnitude in the B -band. We estimate the amount of UV attenuation, A_{UV} , from the UV continuum slope (i.e. if $f_\lambda \propto \lambda^\beta$), following Meurer et al. (1999):

$$A_{\text{UV}} = 4.43 + 1.99\beta. \quad (3)$$

We estimate the UV continuum slope β from the FUV-NUV color (observed $B - I$ color), as detailed in Section 3.3.

3.1.2. SFR from $H\alpha$

Another widely used diagnostic for measuring the SFR is nebular emission, with $H\alpha$ being the most common because it is the strongest of the Balmer H recombination lines, and it is least affected by underlying Balmer stellar absorption features and by extinction compared to the higher-order Balmer lines at shorter wavelengths.

The conversion factor between ionizing flux and the SFR is usually computed using an evolutionary synthesis model. Only stars with masses $\gtrsim 10 M_\odot$ and lifetimes < 20 Myr contribute significantly to the integrated ionizing flux, so the emission lines provide a nearly instantaneous measure of the SFR, independent of the previous star formation history. We again adopt the conversions of Kennicutt (1998) (Salpeter IMF and solar metal abundance), with the assumption that the star formation history is constant for at least the past 10 Myr and that Case B recombination at $T_e = 10000$ K applies. We

modify their calibration downward by a factor of 0.23 dex to match a Chabrier (2003) IMF:

$$\frac{\text{SFR}_{H\alpha}}{M_\odot \text{ yr}^{-1}} = 4.7 \times 10^{-42} \frac{L_{H\alpha,\text{corr}}}{\text{erg s}^{-1}}. \quad (4)$$

where $L_{H\alpha,\text{corr}}$ is the $H\alpha$ luminosity corrected for attenuation, i.e. $L_{H\alpha,\text{corr}} = L_{H\alpha,\text{obs}} \times 10^{0.4A_{H\alpha}}$.

Since $H\alpha$ lies at 6563 Å, it suffers much less dust extinction compared to the UV rest-frame of a galaxy spectrum. On the other hand, the Lyman continuum ionizing radiation that gives rise to the $H\alpha$ emission is mainly produced by massive, short lived stars that are probably deeply embedded in the giant H II regions, whereas less massive ($< 10 M_\odot$) stars still contribute to the UV rest-frame stellar continuum on the long-terms, shine over timescales 10 times longer, and have time to clear or migrate out of the dense H II regions. The net outcome of this process is that $H\alpha$ emission probably suffers from an extra attenuation, parametrised by the f -factor that relates $E(B - V)_{\text{star}} = f \times E(B - V)_{\text{gas}}$.

Moreover, the $H\alpha$ luminosity depends also on the actual extinction in the Lyman continuum, as one gets one $H\alpha$ photon for each Lyman continuum photon that does not get absorbed by a dust grain (see, e.g., Boselli et al. 2009; Puglisi et al. 2016). Since we are unable to constrain the extinction in the Lyman continuum, we absorb this part of physics in the overall uncertainty of the f -factor (see below), which itself is very uncertain since it depends on the actual extinction law (from the optical to the Lyman continuum) and on the geometry of the emitting regions.

The extra amount of attenuation suffered by nebular emission is still debated, especially at high redshifts. In the local universe, the stellar continuum undergoes roughly half of the reddening suffered by the ionized gas, namely $f = 0.44$ (Calzetti et al. 2000). Important to note is that Calzetti et al. (2000) used two different extinction curves for the nebular ($k(\lambda)_{\text{gas}}$; Cardelli et al. 1989; Fitzpatrick 1999) and continuum ($k(\lambda)_{\text{star}}$; Calzetti et al. 2000), which have similar shapes but different normalizations ($R_V = 3.1$ and 4.05, respectively). If not differently noted, we adopt the same extinction curves here. At higher redshifts, Wuyts et al. (2013) present a polynomial function to derive extra attenuation from the continuum attenuation, hence the f value may not necessarily be a constant value for all types of galaxies (see also Price et al. 2014). It is also suggested by recent studies that the typical f value may be higher ($f = 0.5 - 1.0$) for high-redshift galaxies (see, e.g., Erb et al. 2006; Reddy et al. 2010; Kashino et al. 2013; Koyama et al. 2015; Valentino et al. 2015).

In this paper we constrain the attenuation of the $H\alpha$ emission line, $A_{H\alpha}$, by converting the dust attenuation in the continuum at V , A_V , using:

$$\begin{aligned} A_{H\alpha,\text{gas}} &= \frac{E(B - V)_{\text{gas}}}{E(B - V)_{\text{star}}} \cdot \frac{k(H\alpha)_{\text{gas}}}{R_{V,\text{star}}} \cdot A_{V,\text{star}} \\ &= \frac{1}{f} \cdot \frac{2.36}{4.05} \cdot A_{V,\text{star}}, \end{aligned} \quad (5)$$

with $f = E(B - V)_{\text{star}}/E(B - V)_{\text{gas}}$ ($f = 0.44$ from Calzetti et al. 2000 and $f = 0.7$ from, e.g., Kashino et al.

2013). We note that the prescription of Wuyts et al. (2013) gives very similar results to this fiducial relation using a value of $f = 0.44$.

3.2. Effects on (FUV–NUV) color from Stellar Population Variations

In this section we investigate the effect of varying the stellar population properties on the (FUV–NUV) color (see also, e.g., Cortese et al. 2008; Wilkins et al. 2011). To compare the different effects we take a reference model about which we consider deviations in the amount of dust, the previous SFH, metallicity and IMF. This reference model assumes 1 Gyr continuous star formation, solar metallicity ($Z = 0.02$), a Chabrier (2003) IMF, no dust and is constructed using the Bruzual & Charlot (2003) population synthesis model. This scenario suggests a rest-frame (FUV – NUV) color of -0.14 mag.

By far the largest potential effect on the UV color of SFGs is the presence of dust: changing $A_V = 0.0 \rightarrow 0.5$ mag results in $\Delta(\text{FUV} - \text{NUV}) \approx 0.4$ mag. The strong wavelength dependence of typical (e.g., Calzetti et al. 2000) reddening curves results in greater extinction in the UV (relative to the optical or near IR) and the reddening of UV colors. Therefore, reddening of the UV colors provides a good diagnostic of the magnitude of the dust attenuation. Next, we vary the second order stellar population parameter in order to constrain the typical uncertainty that is related to estimating A_V from (FUV – NUV) color.

Variation in the SFH influences the (FUV–NUV) color since after prolonged periods of star formation some fraction of the most-massive stars will have evolved off the stellar main sequence, which reduces the relative contribution of these stars to the UV continuum resulting in a redder color. For example, for a given total stellar mass, reducing the age of a constantly star-forming population by a factor of 10 (i.e. from 1 Gyr to 100 Myr), makes a color by $\Delta(\text{FUV} - \text{NUV}) \approx -0.1$ mag bluer. Lowering the metallicity from $Z = 0.02 \rightarrow 0.004$ results in $\Delta(\text{FUV} - \text{NUV}) \approx -0.1$ mag. Finally, changing the IMF from Chabrier (2003) to Salpeter (1955) makes the color redder by a small amount ($\Delta(\text{FUV} - \text{NUV}) = 0.01$ mag) because Salpeter (1955) IMF is more bottom-heavy. Summarizing, for a given (FUV – NUV) color we estimate the typical uncertainty on A_V due to stellar population differences to be at most ~ 0.2 mag.

3.3. From (FUV–NUV) Color to Dust Attenuation

We derive the (FUV–NUV)– A_V and (FUV–NUV)– β conversions in Appendix A. Briefly, we obtain the conversions by generating a set of model SEDs from Bruzual & Charlot (2003), for six different metallicities ($Z=0.0001, 0.0004, 0.004, 0.008, 0.02$, and 0.05) and three different SFHs (constant, exponentially rising, and exponentially decreasing). We find a tight correlations between the (FUV–NUV) color and A_V and β , which are given by Equations A1 and A3.

3.4. Important Remarks about the Dust Attenuation Correction

Before proceeding we want to highlight some key assumptions behind our results. First, it is well known that the chemical and physical properties and the geometrical distribution of dust within external galaxies are

a major uncertainty in the evaluation of their dust attenuation properties. In the absence of reliable constraints, we are working here within the traditional framework of the uniform screen approximation. From this it follows that the attenuation curves depend solely on wavelength, i.e. details of the dust-star geometry are packaged into the attenuation curve (see, e.g., Penner et al. 2015 and Salmon et al. 2016 for a more detailed discussion).

Concerning the dust geometry, in the local Universe, Liu et al. (2013) analyzed the dust distribution of M83 at a resolved spatial scale of ~ 6 pc, finding a large diversity of absorber/emitter geometric configurations can account for the data, implying a more complex physical structure than the classical foreground dust screen assumption. However, when averaged over scales of $100 - 200$ pc, the extinction becomes consistent with a dust screen, suggesting that other geometries tend to be restricted to more local scales. At high- z , the dust-star geometry of galaxies is still largely unconstrained. Genzel et al. (2013) argued based on a massive $z = 1.53$ SFG that the resolved molecular gas surface density and the resolved attenuation are well modelled by a mixed model of dust and star-forming regions (consistent with Wuyts et al. 2011).

Another question is whether the Calzetti et al. (2000) and Fitzpatrick (1999) attenuation curves for $k(\lambda)_{\text{star}}$ and $k(\lambda)_{\text{gas}}$, respectively, are appropriate for high- z SFGs on resolved scales of ~ 1 kpc (given that they were empirically derived from local galaxies). Moreover, it is uncertain whether the attenuation curve should be universal, given that the conditions which produce the attenuation curve are complex. They depend on the covering factor, dust grain size (which is dependent on metallicity), and line-of-sight geometry; these can therefore change when e.g., galaxies are viewed at different orientations (Witt & Gordon 2000; Chevallard et al. 2013) or have different stellar population ages (Charlot & Fall 2000).

In the local Universe, we know that the attenuation curve is not universal and varies between the Small and Large Magellanic Clouds (SMC and LMC), the Milky Way and star-burst galaxies. At high- z , the attenuation curve is less well constrained (see e.g., Kriek & Conroy 2013; Zeimann et al. 2015; Salmon et al. 2016; Forrest et al. 2016). Reddy et al. (2015) suggest that the attenuation curve for $z \sim 2$ galaxies is lower by 20% in the UV, which leads to SFRs that are $\sim 20\%$ and stellar masses that are 0.16 dex lower. Since our main results are based on the sSFR, some of this effect will cancel out, i.e. we expect that our conclusions will be not significantly affected by this. A detailed analysis of different attenuation curves at different positions within galaxies is beyond the scope of this work and of our data. Therefore, we self-consistently assume the Calzetti et al. (2000) attenuation curve for $k(\lambda)_{\text{star}}$ and Fitzpatrick (1999) for $k(\lambda)_{\text{gas}}$ through this paper, but highlight that this issue is worth investigating in future work.

Finally, regions of total dust obscurations would not be detected in our UV analysis. Compact obscured star-formation has been seen in other samples whose selection criteria, as mentioned in the introduction of this paper, are however clearly very different from ours Tadaki et al. (2015), Barro et al. (2016) and Tadaki et al. (2017). Specifically for our sample, we present below a strong

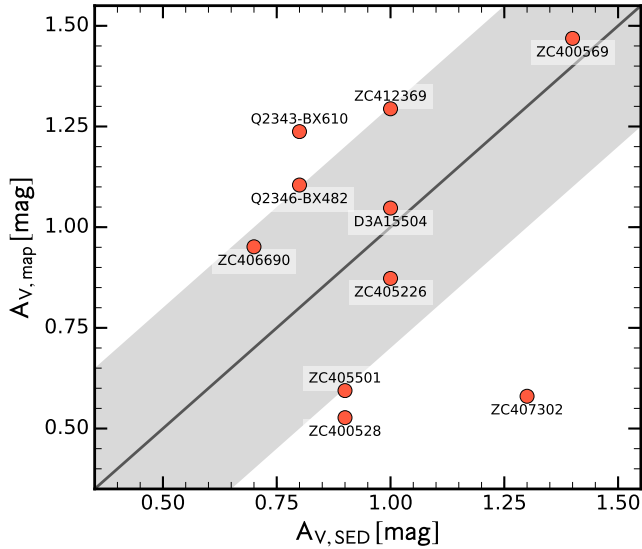


Figure 3. Dust attenuation obtained from the resolved maps ($A_{V,\text{map}}$) versus from the integrated photometry (i.e. SED modelling; $A_{V,\text{SED}}$). The solid black line shows the one-to-one relation. The average difference amounts to -0.01 ± 0.35 mag, i.e. these two estimates are in good agreement with each other. The typical uncertainties are about 0.3 mag.

argument against the presence of totally obscured centers, namely the good agreement between UV and $H\alpha$ integrated SFRs after dust-correction using our dust-attenuation maps, and IR-based SFRs obtained from archival Spitzer and Herschel data.

4. MEASUREMENTS OF DUST ATTENUATION AND SFR IN $Z \sim 2$ SFMS GALAXIES

In this section, we compare integrated values of the attenuation, UV SFR and $H\alpha$ SFR maps with the values from the integrated UV-IR photometry. Furthermore, we present the measurements of the dust attenuation profiles.

4.1. Resolved versus Integrated A_V

In Figure 3 we compare the dust attenuation A_V obtained from our maps ($A_{V,\text{map}}$) with the one obtained from SED modeling ($A_{V,\text{SED}}$), i.e. from the integrated photometry measured in an aperture of $3''$. We derive $A_{V,\text{map}}$ by summing up all pixels within a $3''$ aperture, masking neighboring galaxies, and weighing each pixel according to the flux in the observed *HST* H -band image since this band corresponds to the rest-frame V -band image.

Overall, we find good agreement between $A_{V,\text{map}}$ and $A_{V,\text{SED}}$: the average the difference is -0.01 ± 0.35 mag. Seven of our ten galaxies lie – within the uncertainty – close to the 1-to-1 relation. There are three significant outliers (Q2343-BX610, ZC400528, ZC407302). Both ZC400528 and ZC407302 have close neighbours (see Figure 1) that are masked in the A_V maps but not in the integrated photometry, which can explain the difference. Furthermore the A_V map of Q2343-BX610 shows a large dynamic range, in particular, the center shows a high A_V value of $\gtrsim 2.5$ mag (see below, Figure 5). A_V from integrated photometry tends to miss these high attenuation values.

4.2. SFR from IR versus SFR from UV

The two main SFR indicators used in this paper, the $H\alpha$ recombination line and the UV emission, must be corrected for dust attenuation to recover the intrinsic SFR. In this subsection we use the SFR from IR in order to constrain the intrinsic SFR – and therefore the effect of dust attenuation – with an independent method. The IR is a good SFR indicator since in the limit of high obscuration, most of the UV-optical light from young stars is absorbed and re-emitted into the IR. However, as for other SFR indicators, several assumptions (such as the IMF) must be made to convert the IR luminosity into a SFR (Kennicutt 1998). An important caveat of the IR SFR indicator is that dust can also be heated by older stars and/or AGN. If such dust heating is non-negligible, converting the IR luminosity into a SFR using a standard calibration will overestimate the true SFR (e.g., Sauvage & Thuan 1992; Smith et al. 1994; Kennicutt et al. 2009; Salim et al. 2009; Kelson & Holden 2010; Leroy et al. 2012; Utomo et al. 2014; Hayward et al. 2014).

In Figure 4 (left panel), we compare the dust-corrected UV SFR obtained from our resolved maps ($\text{SFR}_{\text{UV map, corr}}$) both with the integrated UV SFR (SFR_{UV}) and with the integrated UV+IR SFR ($\text{SFR}_{\text{UV+IR}}$). The integrated UV SFR is derived from the UV rest-frame luminosity, according to the relation of Daddi et al. (2004), and adjusted to a Chabrier IMF. For the UV+IR SFR, we follow the approach of Wuyts et al. (2011): we use either UV + PACS for *Herschel* PACS-detected galaxies (PACS Evolutionary Probe (PEP) program; Lutz et al. 2011)¹⁶ or UV + MIPS 24 μm for *Spitzer* MIPS-detected galaxies to compute the sum of the obscured and unobscured SFR. For galaxies lacking an IR detection, the SFR is adopted from the best-fit SED model. The values $\text{SFR}_{\text{UV map}}$ are obtained by summing up the SFR within the $3''$ aperture of the UV SFR map, masking neighboring objects. A direct comparison of the integrated UV SFR and integrated UV+IR SFR, including the upper limits, is shown in Appendix C.

Only one of our ten galaxies (ZC400528) is detected at PACS 100 μm with $\text{SFR}_{\text{UV+100}\mu\text{m}} = 556 M_\odot \text{ yr}^{-1}$. This is a factor ~ 3.8 and ~ 9 larger than the dust-corrected UV SFR estimate from the integrated photometry and map, respectively. As shown in the Appendix B, ZC400528 has a close, but faint neighbour galaxy that is not resolved as an individual source in the *Spitzer* MIPS 24 μm data. Furthermore, this is the only source which is detected with the VLA (Schinnerer et al. 2010) with a 1.4 GHz flux density of 67 μJy that would imply a $\text{SFR} \approx 790 M_\odot \text{ yr}^{-1}$. Together with the nuclear outflow measured in this galaxy (Förster Schreiber et al. 2014), this points to AGN activity. However, it is unclear how much an AGN could contribute to the IR and radio measurements. Hence, this measurement of the UV+IR SFR should be interpreted with caution. Mapping of the dust continuum emission with high spatial resolution will provide further insight in the future.

Four galaxies have been detected in *Spitzer* MIPS 24 μm and we estimated $\text{SFR}_{\text{UV+24}\mu\text{m}}$. For three galaxies (D3A15504, ZC400569, ZC406690), these estimates

¹⁶ Sources have been extracted using deep *Spitzer* MIPS 24 μm source positions as priors.

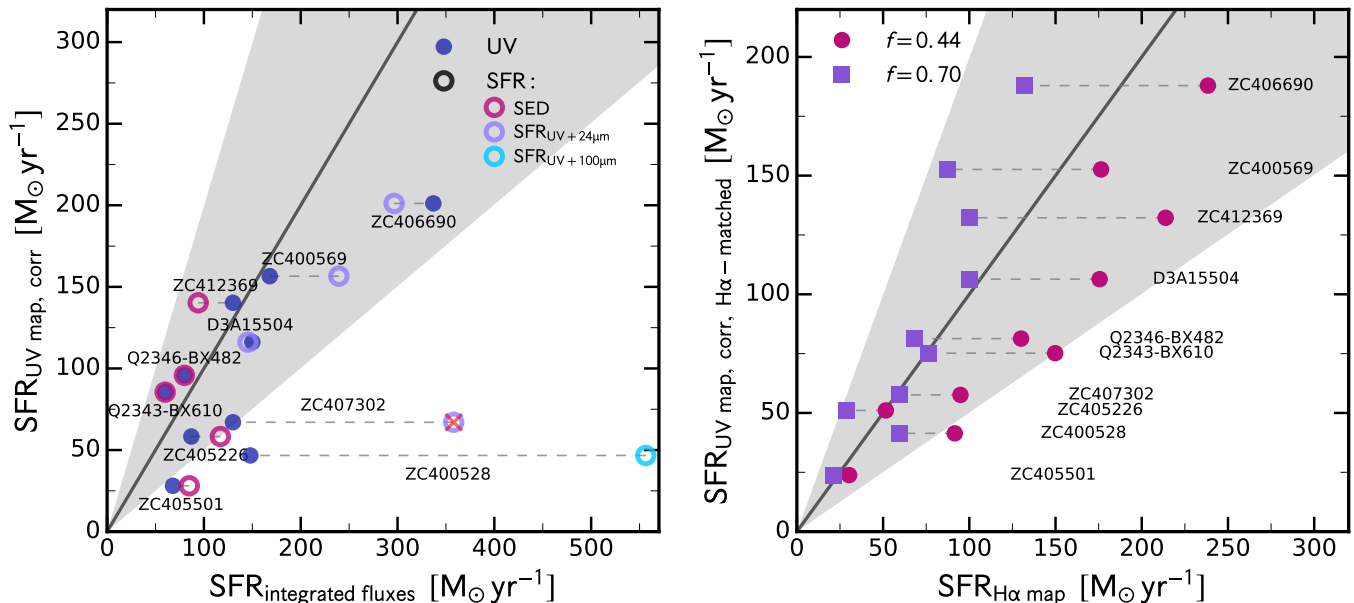


Figure 4. Comparison of different SFR estimates. *Left:* SFR estimated from the dust-corrected UV-SFR map as a function of SFR estimated from integrated fluxes (UV+IR if available and reliable, otherwise SED), measured on the same $3''$ aperture. The black solid line indicates the 1-to-1 relation and the gray shaded area shows the typical 0.3 dex uncertainty. For most galaxies the SFR estimate from the UV-SFR map agrees well with the estimate from the integrated fluxes. Exceptions are ZC400528 and ZC407302: both galaxies have 3-5 times higher SFR predicted from UV+IR than from UV-SFR map. In the case of ZC407302, this can be explained by a neighboring galaxy that contributes significantly to the IR flux. *Right:* SFR estimated from the UV-SFR map as a function of SFR estimated from the $\text{H}\alpha$ -SFR map, measured on the same $\text{H}\alpha$ -based aperture. For each galaxy, we show two different $\text{H}\alpha$ -SFR estimates based on two different attenuation prescriptions: purple circles and violet squares show the $f = 0.44$ and $f = 0.7$ estimates, respectively. The black solid lines indicate the 1-to-1 relation. The UV- and $\text{H}\alpha$ -SFRs agree well within the uncertainties for both attenuation prescriptions with better agreement for the $f = 0.7$ estimates.

agree well with the dust-corrected UV SFR estimates. For one galaxy (ZC407302) the SFR estimated from UV+ $24 \mu\text{m}$ is a factor of three higher than the UV estimate. This is explained by source confusion: ZC407302 has a close, low- z neighbour which contributes significantly to the $24 \mu\text{m}$ flux (see Appendix B). Therefore, we use the dust-corrected UV SFR estimate as the total SFR instead of the UV+IR SFR for this galaxy throughout this paper.

Moreover, three zCOSMOS galaxies (ZC405226, ZC405501, and ZC412369) have no IR-detection at all and therefore the SFR hidden in large amounts of dust is negligible. Finally, two galaxies (Q2343-BX610 and Q2346-BX482) have no IR-coverage. For all galaxies that have been not detected in the IR we can estimate the upper limit on the SFR. The PEP COSMOS field is observed for 200 h to a 3σ depth at $160 \mu\text{m}$ of 10.2 mJy, reaching at $z \sim 2$ IR luminosities of a few times $\sim 10^{12} L_{\odot}$ (SFR about $350 M_{\odot} \text{yr}^{-1}$). A more stringent upper limit can be obtained for the COSMOS MIPS $24 \mu\text{m}$ data: the flux limit of this data is $\sim 80 \mu\text{Jy}$, which corresponds at $z \sim 2$ to a SFR of about $150 M_{\odot} \text{yr}^{-1}$.

Summing up, six of our ten galaxies have only weak or no detection in the IR, two galaxies have no IR-coverage, and two galaxies (ZC400528 and ZC407302) have clearly higher UV+IR SFRs than the dust-corrected UV SFRs. ZC407302 has a boosted IR flux due to its low- z neighbor and we therefore use the dust-corrected UV SFR instead of the UV+IR SFR throughout in this paper. ZC400528 has a faint neighbor and also shows some AGN activity, making the IR flux difficult to interpret. Nevertheless, we use UV+IR SFR as fiducial SFR estimate for this galaxy. Overall, we therefore conclude that, in our sample, there

is no evidence for substantially more star formation hidden by dust relative to what we infer from our dust-corrected, resolved UV and $\text{H}\alpha$ SFRs. This gives us confidence that correcting UV and $\text{H}\alpha$ SFR profiles with the UV-based dust attenuation profiles that we derive in this paper will return reliable estimates of where, spatially-resolved within galaxies, most of the star-formation activity is localised.

4.3. SFR from UV versus SFR from $\text{H}\alpha$

We compare the integrated SFR maps from UV and $\text{H}\alpha$ in Figure 4 (right panel). Since the $\text{H}\alpha$ maps do not extend over the full $3''$ aperture (see Figure 1) we have to match the UV and $\text{H}\alpha$ apertures and PSFs. We define the $\text{H}\alpha$ aperture by the pixels with $\text{S/N} \geq 3$. Clearly, the measured SFR in this aperture is not fully representative of the total SFR, but it is good for the purpose of comparing the UV with the $\text{H}\alpha$ SFR map.

As mentioned in Section 3.3, correcting the $\text{H}\alpha$ SFR estimate for dust attenuation ($A_{\text{H}\alpha, \text{gas}}$; Equation 5) depends on the adopted prescription. In Figure 4 we show the $\text{SFR}_{\text{H}\alpha, \text{map}}$ assuming $f = 0.44$ and $f = 0.70$. Overall, the SFR estimated from UV and $\text{H}\alpha$ agree well. The average log-difference between $\text{SFR}_{\text{UV, map}}$ and $\text{SFR}_{\text{H}\alpha, \text{map}}$ is $0.21^{+0.05}_{-0.13}$ dex and $-0.06^{+0.07}_{-0.14}$ dex for $f = 0.44$ and $f = 0.70$, respectively. The $\text{SFR}_{\text{H}\alpha, \text{map}}$ with $f = 0.70$ slightly under-predicts the $\text{SFR}_{\text{UV, map}}$ values, while the $\text{SFR}_{\text{H}\alpha, \text{map}}$ with $f = 0.44$ slightly over-predicts the $\text{SFR}_{\text{UV, map}}$ values. We use $f = 0.70$ as our fiducial conversion factor for the rest of the paper.

It is actually unclear whether the UV and the $\text{H}\alpha$ SFRs must be the same since they probe different timescales. In particular, as discussed in Section 3.1, $\text{H}\alpha$ probes

mainly $\sim 10^7$ yr old stars, while the UV-derived SFR is somewhat sensitive to the SFH over a ~ 10 times longer interval. Overall, considering the uncertainty from the f -factor together with the possibility of probing the SFRs on different timescales, we find that our $H\alpha$ SFR with both $f = 0.44$ and $f = 0.70$ are in the ballpark with expectations from the UV SFRs.

4.4. PSF-Corrected Dust Attenuation Radial Profiles

To study the variation of extinction within galaxies, we used the rest-frame FUV and NUV (observed B - and I -band) images to construct a two-dimensional (FUV–NUV) color map for each galaxy, following a similar procedure as done in Tacchella et al. (2015b) for estimating the mass surface density distribution from the $J-H$ color map. Since the FUV and NUV observations have different PSFs, we cross-convolved each passband with the PSF of the other passband. To increase the S/N of the color maps in the outer regions of galaxies, where the flux from the sky background is dominant, we performed an adaptive local binning of pixels using a Voronoi tessellation approach, using the publicly available code of Cappellari & Copin (2003). These color maps are then converted to A_V maps using Equation A1, which are shown in Figure 5.

In order to compute the PSF-corrected A_V profiles, we measure the 1D profiles in elliptical apertures with the same ellipticity and center as obtained by the rest-frame optical (observed H -band) image GALFIT fits (Tacchella et al. 2015b). At each radius, the profile value consists of the median of all A_V at that radius. Taking the mean instead of the median does not change the profiles. Furthermore, using the B - and I -band light profiles to derive the color and then the A_V profiles also produces similar results.

These 1D A_V profiles were then fitted with a Sérsic (1968) profile taking into account each galaxy’s PSF. We choose to use a Sérsic function for modeling the A_V profiles simply as a mathematical representation of the data and because the three free parameters in the Sérsic function give a high flexibility. Although the A_V profiles are shallower than the typical galaxy surface brightness profiles (and also the SFR and stellar mass surface density profiles), they are still well described by a Sérsic profile. In order to correct the profiles for deviation from the best-fit single Sérsic model, we derive the residual profile and add this to the best-fit de-convolved Sérsic model, to derive the residual-corrected profiles (Figure 5). Overall, the PSF-convolved model reproduces the data well, with differences $\lesssim 0.2$ mag.

A center of a galaxy must be chosen for constructing a radial profile. We have extensively discussed the influence on the profiles of choosing different centers in Tacchella et al. (2015b), since it sets the foundation for the physical interpretation. In particular, we have highlighted the differences between dynamical, mass-weighted, and light-weighted (rest-frame optical light) centers. For most galaxies, these centers agree with each other (differences are $\lesssim 0.4$ kpc, i.e. $\lesssim 1$ pixel) and we assume the mass-weighted center as our fiducial center. An exception is galaxy ZC406690 that shows a clumpy morphology and for which the center is ambiguous. The kinematic center lies in the center of a ring-like structure, on which the field of view of SINFONI IFU is centered.

The center of mass lies about 5 kpc to the east, on the largest clump visible in Figure 1. For this galaxy, we assume the dynamical center determined from the $H\alpha$ kinematics in order to be consistent with previous studies and to be able to compare the UV and $H\alpha$ emission on scales out to ~ 10 kpc.

Figure 6 shows the individual and stacked A_V profiles as well as $A_{H\alpha}$ profiles. The top panels of Figure 6 show substantial galaxy-to-galaxy variations in the attenuation profiles. The variation in attenuation at a given radius (physical or scaled) amounts to about 1.5 mag for different galaxies. Most galaxies show increasing attenuation profiles within the inner 5 kpc towards the centers, while however a few show the opposite trend. These differences reflect different SFR profiles, as most of the star-formation can happen in star-forming clumps in, near or far away from the galaxy centers.

The stacked profile shows that galaxies have on average an attenuation profile that rises towards the center to ~ 1.8 mag, with a significant amount of dust attenuation (~ 0.6 mag) out to 10 kpc. Wuyts et al. (2012) found a similar decline in star-forming galaxies with $M_\star > 10^{10} M_\odot$ at $0.5 < z < 1.5$, but no explicit radial profiles were presented. Furthermore, these rather weak radial trends agree with local SFGs, where continuum extinction was found from ~ 1.3 mag to ~ 0.8 mag from the center to the optical radius R_{25} (Muñoz-Mateos et al. 2009).

Under the foreground screen assumption A_V is proportional to the dust mass surface density Σ_{dust} , implying a drop of Σ_{dust} by a factor of ~ 3 from the center to 10 kpc ($\sim 3R_M$). On the other hand, stellar mass and star-formation rate surface densities typically fall by a factor of 10 – 100 over the same radial scale (see Section 4.6 and Tacchella et al. 2015a). We discuss this interesting trend further in Section 4.5.

Splitting our sample into two mass bins ($10.0 < \log M_\star/M_\odot < 11.0$ and $11.0 < \log M_\star/M_\odot < 11.5$), we find that there is not a large difference between the two mass bins. As a way of quantifying the slopes and normalizations of the attenuation profiles, we parametrise them with a two-component Sérsic fits (without implying that this specific profile shape bears any physical meaning for the diagnostic in question). The outer (or ‘disk’) component has an $n \approx 0.3 - 0.4$ and $R_e \approx 8$ kpc for both mass bins; the inner (or ‘bulge’) components differ instead for the high- and low-mass bins, yielding respectively $n \approx 0.5$ and $R_e \approx 1.0$ kpc, and $n \approx 0.8$ and $R_e \approx 1.7$ kpc.

Figure 6, bottom panels, show the median dust attenuation of the ionized gas at $H\alpha$, $A_{H\alpha}$. For converting the A_V profiles to $A_{H\alpha}$ profiles we use the procedure described in Section 3.3 and in particular Equation 5. Note that, by construction, using $f = 0.44$ (or, similarly, the prescription of Wuyts et al. 2013) increases of ~ 0.5 mag the attenuation for nebular line regions at $H\alpha$ relative to the stellar continuum at V; for $f = 0.70$ the difference amounts instead to about -0.2 mag.

We compare our profiles with the results of Nelson et al. (2016a) at $z \sim 1.4$, which are based on a Balmer decrement analysis of the stack of several hundred 3D-HST galaxies with masses in the range of $10^{9.8} - 10^{11.0} M_\odot$. Their average $A_{H\alpha}$ profile exhibits a

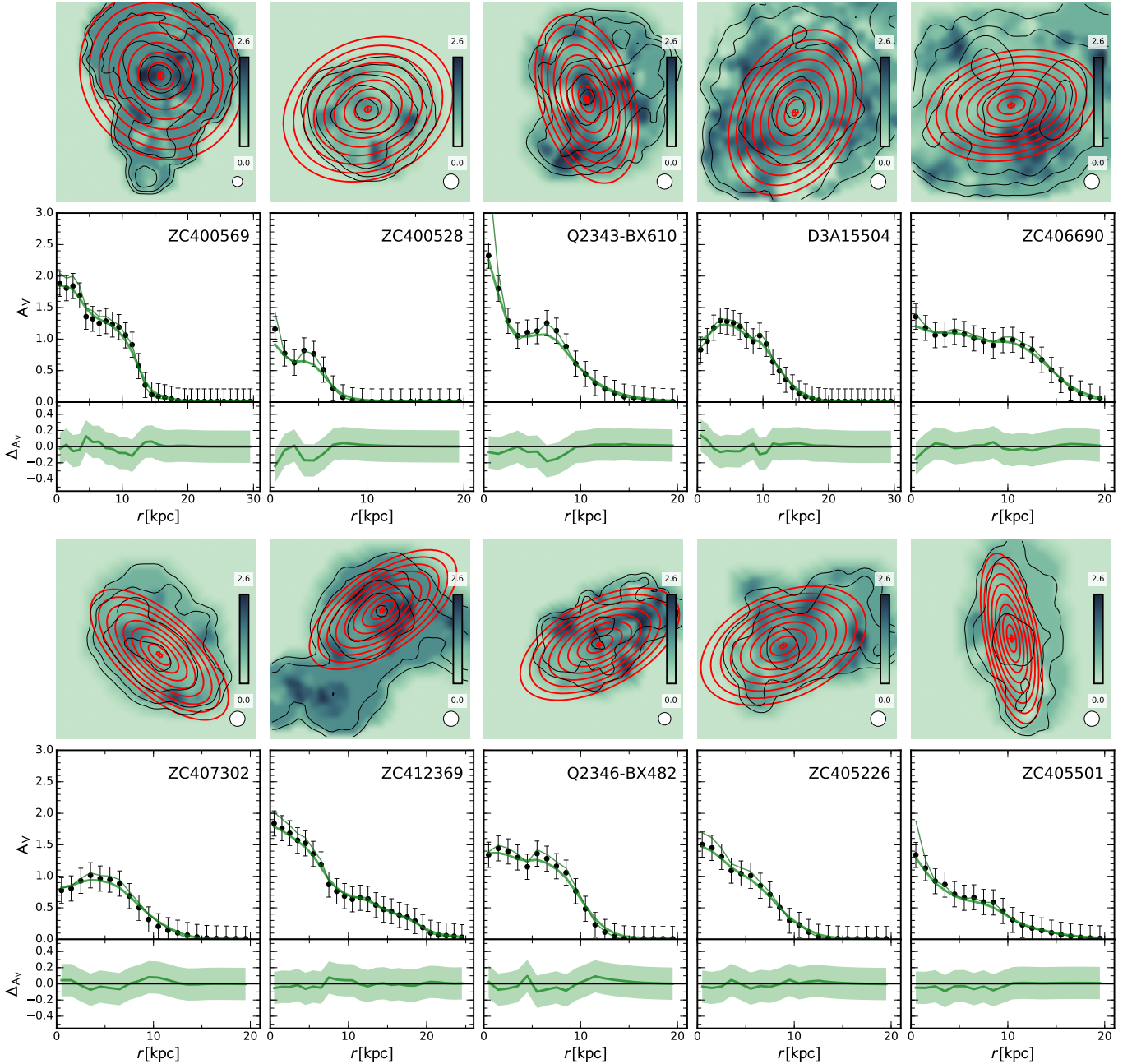


Figure 5. Derivation of the azimuthally averaged dust attenuation A_V profiles. For each galaxy, the top panel shows the A_V map. The red ellipses show the apertures used to construct the azimuthally averaged profile and the contours show the mass distribution. The middle panels show the A_V profiles: the data points with error bars indicate the measured values directly from the A_V map, while the thin and thick green lines show the PSF-corrected and PSF-convolved profiles, respectively. The bottom panels show the difference between the data and the PSF-corrected profiles. The PSF-corrected profiles describe the data well with less than 0.2 mag difference, which is within the estimated uncertainty.

sharp peak in the galaxy center but it is nearly transparent beyond 2 kpc. In the central ~ 1 kpc region, the $A_{H\alpha}$ estimates roughly agree, while the radial trend from the Balmer decrement analysis is much steeper than our slowly declining profiles. In our sample, a single galaxy, Q2343-BX610, substantially increases the average attenuation profile within 2 kpc; excluding this one galaxy makes the central peak in the attenuation profile nearly disappear. This gives a cautionary warning for generalizing to a whole population the results of a stacked analysis, especially for galaxies spanning a broad range

in mass (and thus also size and other properties). Other reasons for the difference between our and their result may arise from contamination from neighboring sources in their sample or the low spectral resolution of the *HST* grism, which blends the [N II] and H α contributions.

4.5. Comparison with A_V Profiles from Simulations

Our analysis above shows slowly falling dust attenuation profiles and thus significant amount of gas in the outer parts of these high- z SFGs if the dust-to-gas ratio is approximately constant. In contrast, the stellar mass and star-formation rate surface densities fall off much

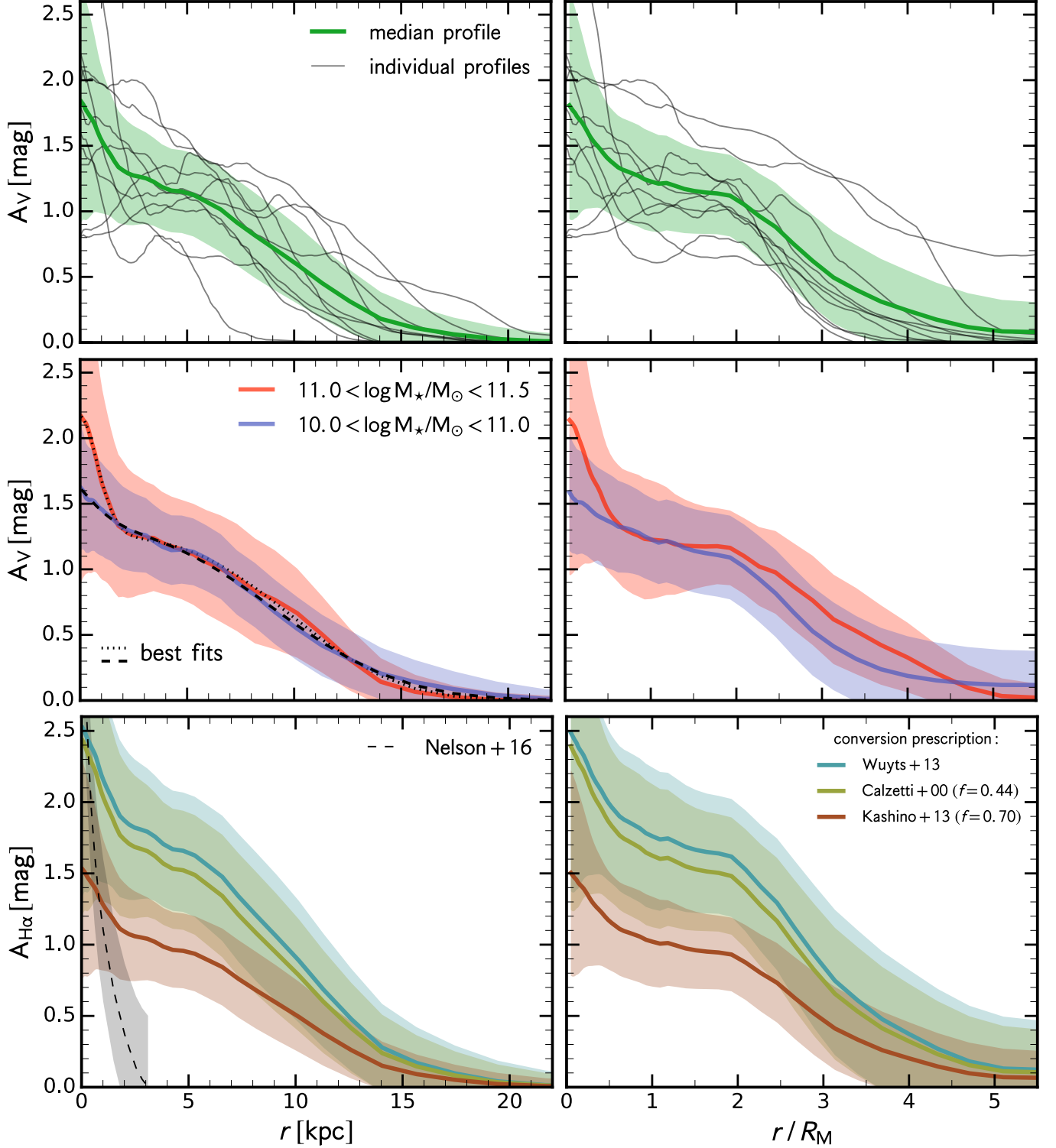


Figure 6. Average dust attenuation profiles. Left panels show the average profiles with radius in physical units of kpc, and right panels show the average profiles in units of radius normalized by the half-mass radius (R_M). In the top panels, the thin grey lines show the individual A_V profiles, highlighting the substantial variety of the attenuation profile from galaxy to galaxy. The green solid lines indicate the average A_V profiles with their 1σ scatter. The center panels show in cyan and orange the average A_V profiles for the lower and higher mass galaxies, respectively. The average A_V profile increases towards the center. The bottom panels show the inferred dust attenuation towards HII regions ($A_{H\alpha}$). The solid lines show the inferred $A_{H\alpha}$ profiles assuming different conversion prescriptions (see legend). The dashed line indicates the recent measurements from the Balmer decrement at $z \sim 1.4$ (Nelson et al. 2016a).

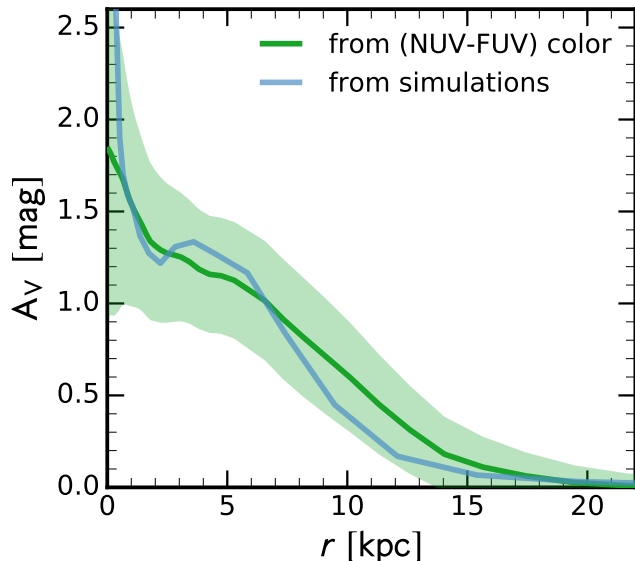


Figure 7. Comparison of our average A_V profile measured from the (FUV–NUV) color (green line) with the A_V profiles derived from gas surface density profiles in cosmological zoom-in simulations (blue line). There is an overall good agreement between observations and simulations within the scatter.

quicker with radius. We investigate this further by comparing our measured dust attenuation A_V profiles with the ones from hydrodynamical cosmological simulations, despite the known issues of them arising from unknown subgrid physics. A way to do so is to convert gas density profiles to dust density profiles and then to dust attenuation A_V profiles, assuming constant conversion factors for (and within) galaxies. Clearly, both conversion steps are uncertain and may depend on galactic properties such as the metallicity and, especially, gas-to-dust ratio, which are not well constrained. Furthermore, converting the dust density profiles to attenuation profiles depends on the geometry of the systems, i.e. how the gas/dust is mixed with stars along the line of sight, as we discussed in Section 3.4. Assuming a constant conversion factor between the gas surface density and dust attenuation as a function of radius may thus be too simplistic and should be further studied in simulations which implement self-consistent radiative transfer modelling.

With these caveats in mind, we nevertheless perform here a comparison with the VELA hydrodynamical zoom-in simulations of Ceverino et al. (2014) and Zolotov et al. (2015), using the simplified approach outlined above, since in these simulations we have already studied in Tacchella et al. 2016a the galaxies’ stellar mass and SFR surface density profiles and found them in good agreement with the observed profiles of Tacchella et al. 2015a, i.e., the decrease from the center to 10 kpc by a factor of about 10 – 100. In order to derive the A_V profiles, we use the cold ($T < 10^4$ K) gas surface density profiles of Tacchella et al. (2016a) (their Figure 9), namely, we use the average surface density of all simulated galaxies with $10.6 < \log M_*/M_\odot < 11.5$ at $z = 1.5 - 3.0$ and a constant conversion factors so that we match the observed A_V value at 1 kpc.

Figure 7 shows the comparison between observed and numerical attenuation profiles. Overall, we find good

agreement, especially after accounting for the large scatter of the profiles for different galaxies. The difference inside 1 kpc is not straightforward to interpret since this is the size of the observed PSF. If real, a possibility is that A_V saturates because of the dust-screen assumption (see Genzel et al. 2013 for an extended discussion on this, in particular their Figure 7).

Figure 7 makes the interesting point that the simulated galaxies have substantial amount of gas in their outskirts, which makes their inferred dust attenuation profiles consistent with the one from observations. Specifically, the gradient of the simulated profiles are only slightly steeper than the observed profiles. Within the discussed caveats, we note that this is encouragingly in the right direction of support for our observed dust attenuation profiles to be physically realistic, given that the gas surface density profiles that produce the simulated dust profiles are self-consistently originated in simulations that also match very well the stellar mass and SFR surface density distributions.

4.6. Radial Star-Formation Rate Density Profiles

With the dust attenuation maps and profiles in hand, we are now able to correct the radial SFR density profiles, improving on the analysis of Tacchella et al. (2015a) where a uniform dust attenuation correction throughout the galaxy was applied. In this section, we present the SFR profiles and how they are affected by different dust attenuation corrections.

In Figure 8 we present the radial $H\alpha$ and UV SFR surface density profiles. We derive the radial SFR surface density profiles in the same way as the aforementioned dust attenuation profiles (see Section 4.4). The $H\alpha$ SFR density profiles for most of the galaxies assuming uniform attenuation have been published in Tacchella et al. (2015a).

Overall, there is a large diversity in the SFR profile shapes. Although on average SFR surface density profiles are well represented by an exponential star-forming disk of different sizes, there is richness of behavior in the individual profiles. Some galaxies have steeper profiles (ZC400528 and ZC412369) or flatter profiles due to bumpy features in the outskirts. The bumpy features can be explained by star-forming clumps in the galaxies’ outskirts. Two exceptional galaxies are Q2346-BX482 and ZC406690 that show nearly flat or even increasing SFR density profiles towards the outskirts. Galaxy Q2346-BX482 has several star-forming clumps at similar galactocentric distances that together surpass the SFR density in the center (see Figure 1). Galaxy ZC406690 shows a reduction in the SFR density in the center. The SFR density peaks at ~ 5 kpc. As mentioned before, this signature must be interpreted with care. We adopted as our fiducial center the kinematic center. Using instead the mass-weighted center (which also coincides with the peak of SFR) would make the profile centrally peaked, i.e. there would be no reduction in SFR towards the center.

We measure a typical inner (< 1 kpc) SFR density of $\Sigma_{\text{SFR}, 1\text{kpc}} \approx 2 - 12 M_\odot \text{ yr}^{-1} \text{ kpc}^{-2}$ for the more massive galaxies in our sample ($11.0 < \log M_*/M_\odot < 11.5$; namely ZC400569, ZC400528, Q2343-BX610, and D3A15504), while the lower mass

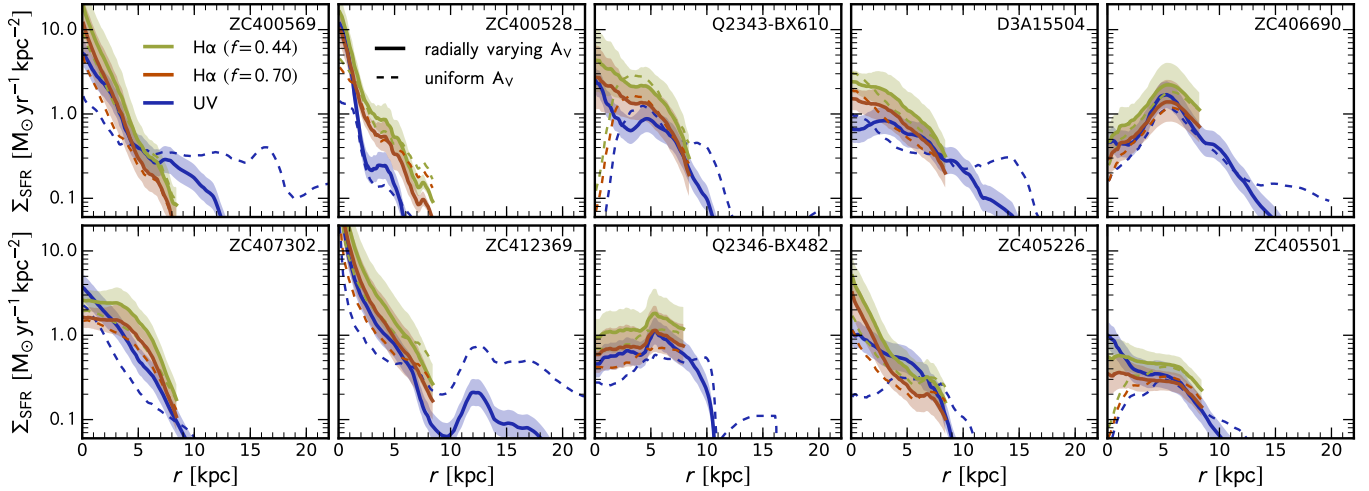


Figure 8. Radial SFR surface density profiles. Each panel shows the profiles for an individual galaxy. The khaki, red and blue lines indicate the SFR estimated from H α with $f = 0.44$, H α with $f = 0.70$, and UV, respectively. The dashed and solid lines show the SFR profiles assuming a uniform dust screen and the radial A_V profiles from Figure 6, respectively. The UV and H α (especially with $f = 0.70$) SFR profiles agree within the uncertainty. Our galaxies have SFR densities in their centers of $0.3 - 20 M_\odot \text{ yr}^{-1} \text{ kpc}^{-2}$. Several galaxies have SFR density peaks in their outskirts that arise from heavily star-forming clumps. Since most of the attenuation profiles are rising towards the centers, the SFR profiles using the radial dependent A_V correction are more centrally concentrated than the SFR using the uniform A_V correction.

galaxies ($10.0 < \log M_*/M_\odot < 11.0$) have $\Sigma_{\text{SFR}, 1\text{kpc}} \approx 0.3 - 3 M_\odot \text{ yr}^{-1} \text{ kpc}^{-2}$. In the lower mass bin, we have excluded ZC412369 with $M_* \approx 3 \times 10^{10} M_\odot$ which is a merger, causing probably the enhanced SFR in the center of $\Sigma_{\text{SFR}, 1\text{kpc}} \approx 20 M_\odot \text{ yr}^{-1} \text{ kpc}^{-2}$.

Focusing now on the difference between H α and UV SFR density profiles, we find overall good agreement between the estimators. As highlighted in Section 4.3, the difference in the overall normalization between H α and UV SFRs depends on the f -factor. With $f = 0.70$, the H α and UV SFRs agree more than with $f = 0.44$.

Since the overall normalization difference between H α and UV is mainly determined by the dust prescription, it may be more compelling to analyze the difference in the profile shapes. For most galaxies, there are small differences in the profile shape. Some galaxies show steeper SFR profiles in H α than in UV (D3A15504, ZC400569, ZC405226), while others show the contrary (Q2343-BX610, ZC400528, ZC405501, ZC407302). More concentrated UV profiles may indicate the progression of the star formation towards the outskirts.

Finally, we can also quantify the difference between using the radially varying A_V profiles versus a uniform A_V value (fiducial assumption in the work of Tacchella et al. 2015a) for correcting the SFR density for dust attenuation. These two different dust corrections are shown with solid and dashed lines, respectively. Since the A_V profiles are increasing towards the centers, it is understandable that correcting the SFR density by those profiles leads to more centrally concentrated SFR density profiles than when using a uniform A_V value. In two cases (Q2343-BX610 and ZC405501), the A_V profiles are so steep that the SFR density profiles reverse, i.e. they are increasing towards the center with the radially varying A_V profiles, while they are decreasing with the uniform A_V value.

5. DISCUSSION

5.1. The making of massive spheroids on the $z \sim 2$ star-forming Main Sequence

The SFR profiles presented in Section 4.6 inform us on the location where $z \sim 2$ SFMS galaxies sustain their high SFRs. The newly formed stars might be however in principle a negligible contribution to the local stellar mass density relative to the stellar density already in place. To understand whether these galaxies are caught in the act of changing their structural classification properties (i.e. by increasing their central mass concentration thereby forming their bulge components, or increasing their stellar mass density at large radii thereby growing the sizes of their disk components) we switch to a diagnostic that is able to trace the change in shape of the stellar mass profiles, i.e. the sSFR profile defined as:

$$\text{sSFR}(r) = \Sigma_{\text{SFR}}(r) / \Sigma_M(r) \quad (6)$$

where Σ_{SFR} is the SFR surface density profile and Σ_M is the stellar mass surface density profile. With our definition of stellar mass as the integral of the past SFR, sSFR gives directly the inverse of the mass e -folding (i.e. roughly the mass doubling) timescale.

These sSFR profiles are shown in Figure 9. The top and bottom panels show the sSFR based on the UV and H α SFR, respectively. We show the individual profiles as well as the stacked profiles in mass bins given by $10.0 < \log M_*/M_\odot < 11.0$ and $11.0 < \log M_*/M_\odot < 11.5$. There is a wide range of shapes in the individual profiles, especially in the innermost and outermost regions, but the overall trend is that lower mass galaxies have on average flat sSFR profiles, and high mass galaxies have centrally-suppressed sSFR profiles. The H α and the UV SFR tracers agree well with each other and reproduce this same result.

Most importantly, these results stand true not only when adopting the radially-constant attenuation profiles, but also with the newly-derived radially-varying dust attenuation corrections. Quantitatively, there are of course differences. Most evident is the difference in the lower mass bin for the UV-based profiles: the radially-constant dust correction gives an outward-increasing sSFR profile;

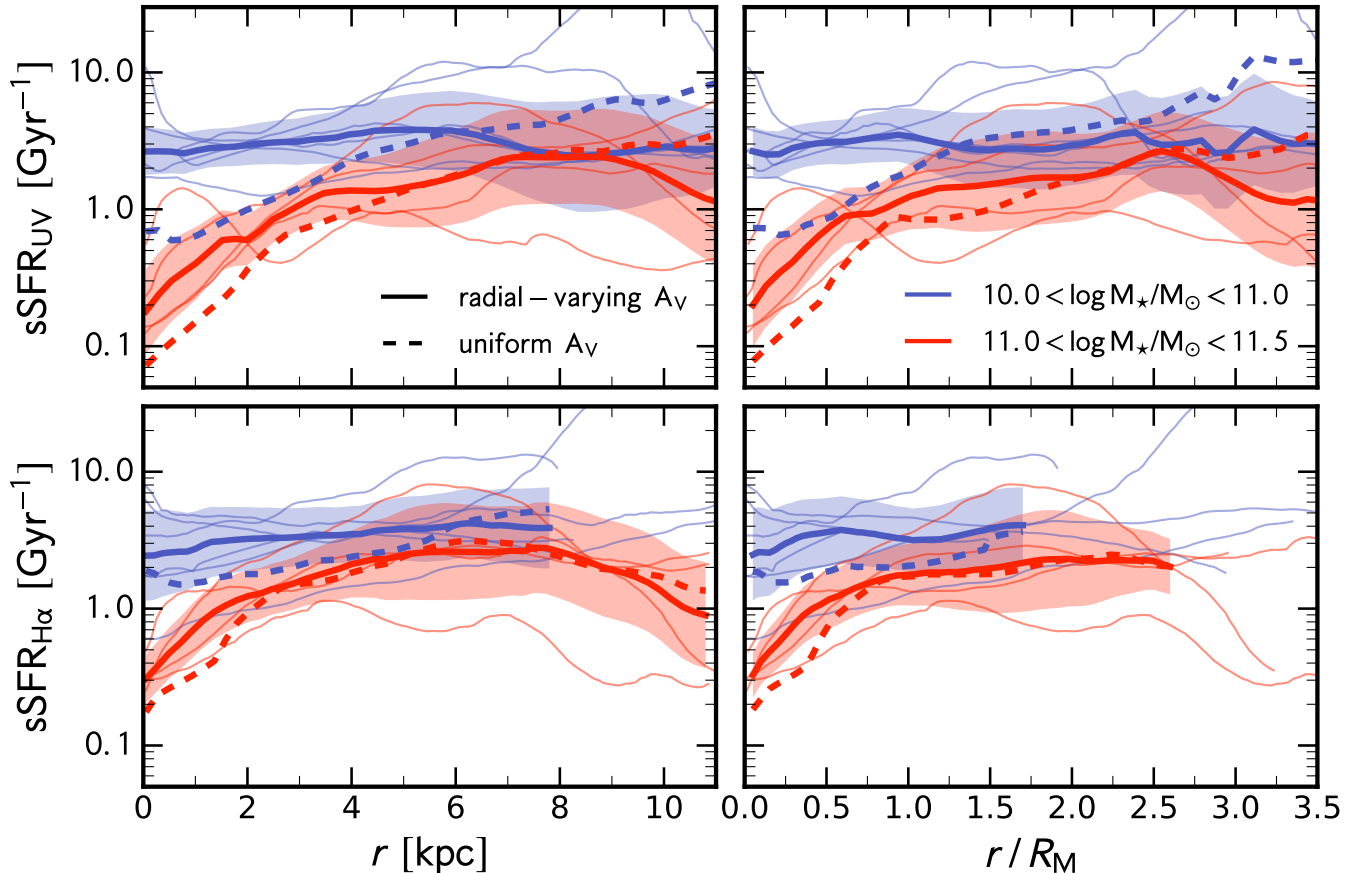


Figure 9. The sSFR profiles from UV (top) and H α (assuming $f = 0.70$; bottom) are shown as a function of radius in physical units (left) and scaled by the half-mass radius R_M (right). The color coding shows the two mass bins. The thin lines show the individual galaxies, while the solid and dashed lines show the average profiles dust-corrected respectively using the radially-varying attenuation profiles and the uniform dust screen model. The radially-varying attenuation correction increases the sSFR in the central regions, but there is only little change in the overall sSFR profiles’ shapes. Nevertheless, in massive galaxies these profiles remain centrally-suppressed relative to the galaxies outskirts.

introducing the measured radial dependence for the dust correction leads to a flat sSFR profile. A flat sSFR profile is also what is observed in H α , which emphasizes the importance of implementing the radial-dependent dust correction to the UV indicators in order to bring the two to agreement.

The fact that lower mass galaxies have flat sSFR profiles and high mass galaxies have centrally-suppressed sSFR profiles, even when radial variations of dust attenuation are accounted for, is a result of significance: it confirms that, below the mass scale of $\sim 10^{11} M_\odot$, SFGs on the SFMS at $z \sim 2$ are vigorously doubling their stellar mass at a similar pace in their inner (‘bulge’) and outer (‘disk’) regions. In contrast, (at least some of) the most massive of them sustain their high SFRs in their outer disks and host almost-quenched inner ‘bulges’, as already pointed out in Tacchella et al. (2015a). This agrees well with the observations that, at all epochs, SFGs grow on an almost time-independent correlation between stellar density within the central kpc and total stellar mass (dubbed “structural Main Sequence” by Barro et al. 2015), until they reach a mass of order $\sim 10^{11} M_\odot$ when quenching intervenes (Tacchella et al. 2015a).

More in detail, at $\log M_*/M_\odot < 11.0$ we measure on average a sSFR value of $\langle \text{sSFR} \rangle \approx 3 \text{ Gyr}^{-1}$, which is

consistent with the sSFR value of the SFMS at $z \sim 2.2$ at this mass scale (e.g., Rodighiero et al. 2014; Whitaker et al. 2014; Schreiber et al. 2015). In contrast the higher mass galaxies $\log M_*/M_\odot > 11.0$ have on average sSFR values which range from $\langle \text{sSFR}_{\text{out}} \rangle \approx 2 \text{ Gyr}^{-1}$ at large radii ($\gtrsim 4 \text{ kpc}$ or $\gtrsim 1 R_M$), again consistent with the SFMS estimates quoted above, to nearly one order of magnitude lower, $\langle \text{sSFR}_{\text{in}} \rangle \approx 0.1 - 0.4 \text{ Gyr}^{-1}$ in the inner bulge regions. This low inner sSFR value implies a mass-doubling time of $\sim 2.5 - 10.0 \text{ Gyr}$, which is comparable to or larger than the Hubble time at $z \sim 2$. The star-formation activity that is taking place in the centers of these galaxies will therefore not significantly increase the central stellar mass density in these systems: their dense bulge components are already in place, as also argued in Tacchella et al. (2015a). The direct comparison of the UV- and H α -based sSFR profiles show not only a qualitative but also a quantitative agreement for the values above.

Our findings for the sSFR profiles have also implications for the evolution of the size-mass relation of galaxies, and for identifying the main physical drivers behind this evolution. The fact that at masses below and above $\log M_*/M_\odot \sim 11.0$ the radial sSFR profiles are respectively flat and outward-increasing is overall consistent with studies of the average size growth of the SFG pop-

ulation which. In the $\log M_*/M_\odot < 11.0$ mass regime, find a slower evolution with cosmic time, and a shallower slope for the mass-size relation at any epoch, relative to the higher mass population (e.g., Shen et al. 2003; Franx et al. 2008; van Dokkum et al. 2008; Cassata et al. 2013; Cibinel et al. 2013; Mosleh et al. 2011; Newman et al. 2012; Carollo et al. 2013; Belli et al. 2014). Furthermore, the almost-quenched cores of the more massive galaxies in our sample are a strong argument for progenitor bias effects being a major driver of the observed size evolution of the $\sim 10^{11} M_\odot$ quenched population (Carollo et al. 2013; Fagioli et al. 2016).

As shown in Tacchella et al. (2015a), these galaxies have saturated their stellar mass densities within several kpc to the values that are observed in the $z = 0$ spheroid population of similar mass. The key result that we report in this paper is that obscuration by dust is not responsible for the low SFR in their cores, and thus the quantification of their inner sSFR, which demonstrates that only a negligible amount of mass will be added to their inner regions in their subsequent evolution. This implies that these galaxies, that will soon leave the SFMS to reach their final resting place on the quenched sequence, will do so bringing with them, already in place, the high inner stellar densities that we identify with the $\sim 10^{11} M_\odot$ spheroid population in the local Universe. Direct quenching from the SFMS to the red and dead cloud should be no surprise at the mass scales that we are discussing. Indeed, the bulk of the spheroid population around $M_* \sim 10^{11} M_\odot$ shows all signs of a highly dissipative formation history, i.e. disk isophotes (Bender et al. 1988), cuspy nuclei (Faber et al. 1997), outer disks (Rix et al. 1999), generally a high degree of rotational support (Cappellari 2016), and steep metallicity gradients (Carollo et al. 1993). We note that this is in contrast with the ultra-massive spheroid population at $M_* \gg 10^{11} M_\odot$: such ultra-massive spheroids are very rare and, as already commented in the Introduction (see references there), bear the clear signs that dissipationless processes such as dry mergers must characterize their assembly (see Carollo et al. 2013; Fagioli et al. 2016 for extensive discussions on the $M_* \sim 10^{11} M_\odot$ mass threshold separating quenched spheroids with dissipative properties from more massive counterparts with dissipationless properties).

The evidence for a direct quenching channel of $\sim 10^{11} M_\odot$ galaxies from the SFMS to the quenched population supports the picture in which, at any epoch, the Universe keeps adding, to the red and dead population, quenched galaxies which inherit the properties – including the sizes – of their progenitors on the SFMS (Carollo et al. 2013; Fagioli et al. 2016). Since SFG sizes are seen to roughly scale similarly to the host halos with $(1+z)^{-1}$ (Oesch et al. 2010; Mosleh et al. 2011; Newman et al. 2012; Somerville et al. 2017), this ‘progenitor bias’ effect, i.e. the addition of larger and larger quenched galaxies to the overall population, becomes therefore a major contribution to the observed size growth of the quenched population with cosmic time. The smaller sizes at any given epoch of quenched galaxies relative to SFGs have been shown to be well explained precisely by the cumulative effects of progenitor bias that piles on the quenched population earlier generations of SFGs (Lilly

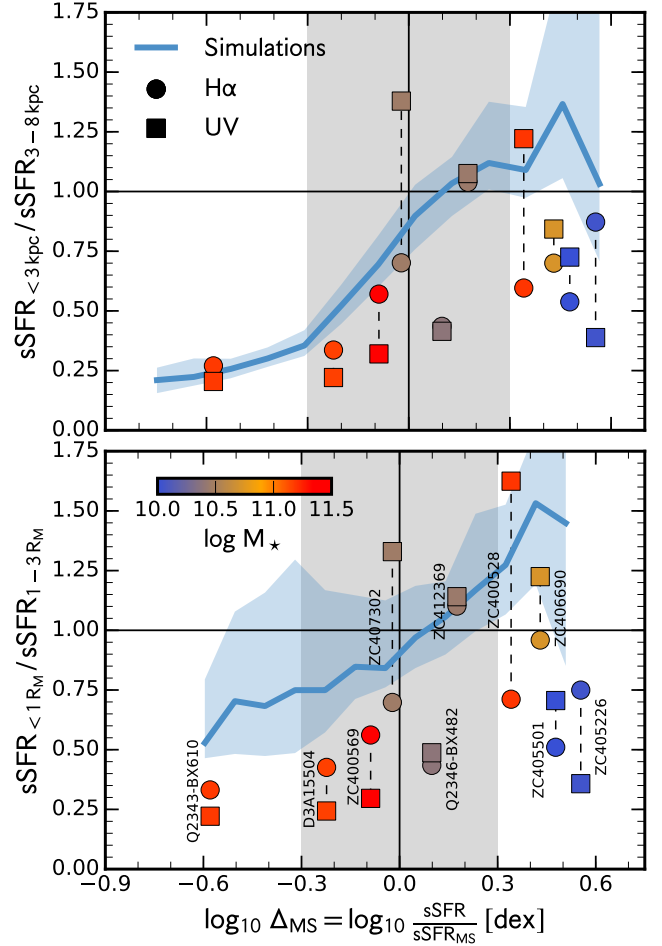


Figure 10. Ratio of the sSFR in the galaxies’ centers and outskirts ($\text{sSFR}_{\text{in}}/\text{sSFR}_{\text{out}}$) as a function of the distance from the SFMS. The top panel shows $\text{sSFR}_{\text{in}}/\text{sSFR}_{\text{out}}$ in physical units (‘in’ measured in the 0–3 kpc range, and ‘out’ in the 3–8 kpc); the bottom panel shows the same quantities computed in radial ranges normalized to half-mass radius, R_M (respectively, within 0–1 R_M and 1–3 R_M). The round and square symbols show the sSFR estimated from H α ($f = 0.70$) and UV, respectively. The color coding shows the total stellar mass. The overall trend for a $\text{sSFR}_{\text{in}} \gtrsim \text{sSFR}_{\text{out}}$ at the upper envelope of the SFMS, and viceversa at its bottom envelope, is also found in cosmological simulations and there is seen to happen due to bulge-forming ‘compaction’ (upper envelope) and disk-forming central depletion (lower envelope) events (Tacchella et al. 2016b).

& Carollo 2016), coupled with the fading of the stellar populations in the disks, once also these outer galactic components exhaust their star-formation activity (Carollo et al. 2016).

5.2. Evidence for bulge and disk growth on the upper and lower envelope of the SFMS

With dust-corrected sSFR profiles in hand, we can turn to ask whether these show any difference depending on where the galaxies lie on the SFMS, not simply ‘along’ the sequence, i.e. as a function of stellar mass (discussed before), but ‘across’ the sequence, i.e. above and below the SFMS ridgeline. Numerical simulations make predictions on what happens to a galaxy as it grows its mass along the SFMS, with observational consequences, which we can test with our data. In particular, Tacchella et al. (2016b) find that, in cosmological zoom-in hydrodynam-

ical simulations (i.e. the VELA suit of Ceverino et al. 2014), SFGs oscillate up and down the average SFMS, reaching the upper envelope when gas vigorously flows towards the galaxy centers where it reaches very high densities. This phase, dubbed ‘compaction’ in Zolotov et al. (2015) (see also Tacchella et al. 2016a,b), leads to a strong central starburst; it is this starburst that pushes galaxies towards the upper SFMS envelope. The starburst adds substantial stellar mass in the galaxy centers, i.e. to the bulge component. Following the compaction phase, SFGs deplete of gas in the centers due to the combination of gas consumption into stars and strong outflows from stellar feedback. This indeed halt the compaction phase, and push galaxies down towards the lower envelope of the SFMS.

The testable prediction of this scenario is that the spatial distribution of the sSFR within galaxies should correlated with their position on the SFMS: galaxies above (below) the SFMS ridge should have a higher (lower) sSFR in their centers than in their outskirts.

In Figure 10 we plot the ratio of the sSFR in the centers and in the outskirts ($\text{sSFR}_{\text{in}}/\text{sSFR}_{\text{out}}$) as a function of the distance from the SFMS (Δ_{MS}). The distance from the SFMS is defined as log-difference of the sSFR of the galaxy to the one of the average SFMS, for which we use a simple linear fit to our sample. The latter agrees well with the SFMS estimates of, e.g., Whitaker et al. (2014) and Schreiber et al. (2015). For the SFR of the SFMS we adopt the total UV+IR SFR that we discuss in Section 4.2. To separate the ‘center’ and ‘outskirts’ of the galaxies, we use two different definitions, one in terms of an absolute physical threshold in radius, and the other in terms of radius normalized by the half-mass radius R_{M} . We plot in the upper panel the inner vs. outer sSFR ratio as a function of radius in physical units in kpc, specifically adopting a 3 kpc threshold to separate inner and outer regions. In the bottom panel we plot instead the same ratio as a function of normalized radius, specifically adopting 1 R_{M} as the separating threshold.

Overall, we observe that galaxies in our sample which lie above the average SFMS ($\Delta_{\text{MS}} > 0.0$) have a higher or at least comparable sSFR in their centers than in their outskirts ($\text{sSFR}_{\text{in}} \gtrsim \text{sSFR}_{\text{out}}$); in contrast, we observe the opposite for galaxies below the average SFMS. This result is robust and our results and conclusions do not change when using both physical and normalized units, when varying the boundaries of the definition of ‘center’ and ‘outskirts’, i.e. using as the separating threshold a value between 1 – 5 kpc in absolute radius units, or 0.5 – 1.5 R_{M} in normalized radius units, and also when changing the SFR indicator, i.e. using our dust-corrected UV or H α instead of the UV+IR SFR that is adopted as fiducial in the plots.

Of course we must exercise care in commenting on this trend, since our galaxy sample is small, and even smaller are thus the below- and above-SFMS subsamples that we are studying. Our (small) sub-SFMS galaxy sample is furthermore dominated by the most massive galaxies ($M_{\star} \gtrsim 10^{11} M_{\odot}$), which are most probably on the way to be quenched. The sSFR ratio vs. Δ_{MS} relation is however not solely driven by stellar mass. The trend of higher sSFR in the center vs outskirt depends more strongly on the distance from the Main Sequence ridge-line than on stellar mass: the Pearson correlation coeffi-

cient is $R = 0.44$ (0.56) for UV (H α) sSFR ratio versus distance from the Main Sequence and $R = -0.09$ (-0.27) for UV (H α) sSFR ratio versus stellar mass.

ZC400528 is very massive, but has a rather flat (or possibly outward declining) sSFR profile and does lie slightly above the average SFMS, in full agreement with the global trend between inner vs. outer sSFR ratio and Δ_{MS} that is traced by the rest of our sample. A suggestive thing that we notice for this galaxy is that its UV-based inner-sSFR is significantly higher than its H α -based inner-sSFR. Interpreting this fact at face value we deduce that this galaxy is currently reducing its sSFR in its inner regions (more than in its outskirts), which decreases its total SFR and suggests that this galaxy, as the other massive SFGs in our sample, has started its descent on the quenching path from its inner regions (as generally argued in Tacchella et al. 2015a). Another galaxy that makes the point that sSFR ratio vs. Δ_{MS} relation is not solely driven by stellar mass is Q2346-BX482, which has a low mass but higher sSFR in its outskirts than in its center.

We have highlighted in Section 2.1 that our sample traces the SFMS. Although stemming from an H α flux selected sample, it may not include the tail of very dusty, IR-bright objects, mainly because of the small number of galaxies in our sample. These IR-bright have been recently studied with ALMA by Silverman et al. (2015), Barro et al. (2016), and Tadaki et al. (2017). Those galaxies lie on the upper envelope or even above the SFMS. Interestingly, these observations point the heavily star-forming centers, i.e. the sSFR profiles are rising toward the centers, which fully consistent with the framework presented here.

Within the caveats of working with a 10-galaxies sample, we do find thus evidence for galaxies growing their inner bulge and outer disk regions as reported from the simulations: they appear to oscillate about the average SFMS in cycles of central gas compaction, which leads to bulge formation, and subsequent central depletion due to feedback from the starburst resulting from the compaction (Zolotov et al. 2015; Tacchella et al. 2016a,b). Furthermore, in these models, full quenching occurs in massive ($M_{\text{vir}} > 10^{11.5} M_{\odot}$), where the hot halo gas suppresses gas supply and gas replenishment time is long compared to the depletion time.

6. SUMMARY AND CONCLUDING REMARKS

The combination of *HST* rest-frame optical, near-UV and far-UV imaging with *VLT* SINFONI AO integral field spectroscopy in 10 massive SFMS galaxies at $z \sim 2.2$, all resolved on scales of ~ 1 kpc, has enabled the derivation of two-dimensional distributions of dust attenuation, and thus dust-corrected star formation rates as well as dust-corrected UV and H α SFR profiles.

The radial profiles of dust attenuation A_{V} vary substantially from galaxy to galaxy, but overall show a general trend to increase towards the galaxy centers, as also found in other samples (Wuyts et al. 2012; Hemmati et al. 2015; Nelson et al. 2016a; Wang et al. submitted). In our work we find only a very weak dependence of the A_{V} profile’s shape on the total stellar mass, with more massive galaxies showing a slightly higher attenuation in their centers than lower mass galaxies. In contrast with studies which report a very steep radial gradient in at-

tenuation parameter, however, our sample displays a relatively shallow gradient, leading to a significant amount of dust attenuation out to large galactocentric distances: at ~ 10 kpc, the average A_V value is ≈ 0.6 mag, which agrees with straightforward predictions of cosmological simulations.

Using these derived radial profiles of attenuation to correct the radial profiles of SFR density, we find that the SFR (and the stellar mass density) profiles fall steeply (by a factor of 10 – 100 from the center to 10 kpc in the outskirts) in contrast to the A_V profiles that fall only mildly (by a factor of ~ 3). In cosmological zoom-in simulations, we find a very similar behavior: the cold ($T < 10^4$ K) gas surface density profiles fall slowly whereas the SFR and stellar mass surface density profiles fall steeply. Assuming a constant gas-to-dust conversion ratio and a simple foreground screen to convert these gas surface density profiles to A_V profiles yield very good agreement our observed A_V profiles. This steep fall in SFR density together with a slow fall in gas density implies a $n \approx 2-4$ in the $\text{SFR} \propto \Sigma_{\text{gas}}^n$ Kennicutt-Schmidt relation (Schmidt 1959; Kennicutt 1989, 1998). Observations of the local spatially resolved galaxies exhibit the same trend: Bigiel et al. (2008) find a nearly linear relation between SFR and molecular gas surface densities, while the power-law index for the relation between SFR and total gas surface densities are significantly steeper, ranging up to 3. Furthermore, in the simulations, this high power-law index can partially be explained by the definition of the gas mass, since here we refer to ‘gas’ as all the cold gas with $T < 10^4$ K, including molecular H_2 , neutral H I as well as ionized H II .

The radial profiles of sSFR reveals an important trend with stellar mass. SFMS galaxies at $z \sim 2$ with masses below $\sim 10^{11} M_\odot$ are on average doubling their stellar mass at a similar pace in their inner and outer regions, indicating that they are synchronously growing their ‘bulge’ and ‘disk’ regions. This agrees well with the observations that, at all epochs, SFGs on the SFMS grow on an almost time-independent correlation between stellar density within the central kpc (Σ_1) and total stellar mass (M_\star) – until, as further discussed below, they reach a mass of order $\sim 10^{11} M_\odot$ at which they start their transition towards the quenched population (see also Tacchella et al. 2015a). The existence of the $\Sigma_1 - M_\star$ relation has also been reported by Saracco et al. (2012) and Barro et al. 2015.

At higher masses, at and above $\sim 10^{11} M_\odot$, using the radially-varying attenuation profiles that we derive in this paper lead to a smaller decrease in sSFR density in the galaxy centers relative to our previous estimates based on a radially-constant A_V value. Importantly however, the use of newly-derived radially-varying dust attenuation profiles still gives for the most massive galaxies SFR density profiles which are ‘centrally depleted’, i.e. star-formation activity in the centers of these massive galaxies is suppressed with respect to their outskirts. The mass-doubling time in the center of these galaxies exceeds the Hubble time by about a factor of two ($\text{sSFR}^{-1} > t_H$), in agreement with the main result of Tacchella et al. (2015a). In that paper we interpreted such centrally-depleted sSFR profiles of massive galaxies as a signature of ‘inside-out quenching’. Here we ex-

tend the range of possible scenarios to include ‘inside-out growth’ of massive galaxies (as, e.g., in Nelson et al. 2016b; Lilly & Carollo 2016). Important is however that dust is not responsible for the observed central depletion of sSFR in the most massive galaxies on the SFMS at $z \sim 2$: these galaxies have genuinely started their descent towards the stockpile of the passively-evolving quenched population and, whether by the nature of galaxy growth or by the onset of a quenching mechanism, they are switching off in an ‘inside-out’ manner. This is consistent with quantitative predictions based on the observed evolutions of the cosmic SFR density and SFMS for the presence of quenched bulges in the cores of star-forming disks at high redshifts (Renzini 2016).

Interestingly, since the inner stellar mass densities of these $z \sim 2$ SFMS massive galaxies are saturated to those of similar mass quenched spheroids in the local Universe (Tacchella et al. 2015a), full cessation of star-formation in these massive galaxies will leave as relics galaxies that, at $z = 0$, will be members of the red-and-dead cloud with a spheroid morphology. This argues for a ‘direct-quenching’ channel, at any epoch, from the SFMS to the quenched population, highlighting the crucial role of progenitor bias effects in driving most of the apparent evolution with cosmic time of the quenched population (Carollo et al. 2013; Fagioli et al. 2016).

The observed concurrent growth on average at $M_\star < 10^{11} M_\odot$ is consistent with cosmological zoom-in simulations, where flat sSFR are found as well. At higher masses, the simulated sSFR profiles are also centrally suppressed with respect to the outskirts. In the simulations, this arises because of gas compaction that triggers a central starburst, which produces a compact core and then leads to central gas depletion and quenching.

Also suggestively, galaxies above and below the average SFMS relation appear to have respectively centrally-enhanced and centrally-suppressed sSFRs. This agrees with a picture, pushed by numerical simulations, where galaxies above the average SFMS ridge are growing their ‘bulge’ components, and those below the average SFMS ridge are growing their outer ‘disk’ components. Specifically, Tacchella et al. (2016a,b) find that galaxies in their simulations oscillate with cosmic time up and down the corresponding average SFMS ridge through alternate phases of gas ‘compaction’, which lead to bulge formation, followed by fast inner gas consumption and/or gas expulsion due to feedback. Our observations offer support to this scenario.

In concluding we emphasise pluses and minuses of the work we have presented. On the positive side, rest-frame FUV, NUV and optical *HST* imaging together with resolved $\text{H}\alpha$ spectroscopy at a similar kpc-resolution give us a unique dataset to learn about the stellar mass distributions within galaxies and the locally-related dust-corrected SFR indicators from two independent diagnostics. By comparison, simple color-color diagrams such as the UVJ diagram (e.g., Labbé et al. 2005; Wuyts et al. 2007; Williams et al. 2009) return sSFR and dust attenuation constraints which are severely affected by the assumption on the adopted stellar population history models: the combination of our *measured* dust attenuation A_V and sSFR profiles would lead to a radial track in the UVJ diagram that, with traditional ‘ τ -models’, would be erroneously attributed to a gradient in dust attenuation.

On the side of caveats, it is important to remember the by-necessity simplified assumptions on dust distribution and properties that we discussed in Section 3.4. Also, our attenuation distributions, resolved on ~ 1 kpc scales within individual SFMS $z \sim 2$ galaxies, are limited to only ten of such systems. We also point out that, in order to obtain the attenuation values A_V and $A_{H\alpha}$, we have used average relations which are well suited for application to large statistical studies of SFGs, but should be used with caution on a galaxy-by-galaxy basis. Finally, while the comparison with IR-based SFR disfavours the presence of regions of total obscurations in our sample, full proof of this will need high resolution imaging of the molecular gas and of the continuum dust emission with f.e. ALMA.

All in all, clearly it will be important to reassess the trends found in this study with larger samples; furthermore, in order to understand the statistical frequency of galaxies with and without totally obscured regions (in particular, cores), the larger samples must be as unbiased as possible in their selection criteria, and be studied with spatially-resolved data across the whole wavelength region, from the UV to the IR. Much work thus lies still ahead to improve on the current state-of-the-art of our knowledge of the impact of dust effects in the interpretation of data for distant galaxies, on which relies our understanding of their star-formation activity and quenching.

We thank the anonymous referee for their comments which improved our original manuscript. We thank Marc Rafeski for providing us his improved dark calibrations for the reduction of the WFC3/UVIS data (Rafelski et al. 2015), and Sandy Faber for inspiring discussions. ST thanks also Jonathan Freundlich, Nicholas Lee, Gabriele Pezzulli, Romain Teyssier, Benny Trakhtenbrot and Weichen Wang for useful suggestions. We acknowledge generous support by the Swiss National Science Foundation. This work was partly supported by the grants ISF 124/12, I-CORE Program of the PBC/ISF 1829/12, BSF 2014-273, PICS 2015-18, and NSF AST-1405962. This research made use of NASA's Astrophysics Data System (ADS), the arXiv.org preprint server, the Python plotting library `matplotlib` (Hunter 2007), and `astropy`, a community-developed core Python package for Astronomy (Astropy Collaboration et al. 2013).

Facility: HST (WFC3, ACS), VLT (SINFONI)

REFERENCES

- Anderson, J., & Bedin, L. R. 2010, *PASP*, 122, 1035 [2.3.1]
 Astropy Collaboration, Robitaille, T. P., Tollerud, E. J., et al. 2013, *A&A*, 558, A33 [6]
 Barro, G., Faber, S. M., Koo, D. C., et al. 2015, *ArXiv e-prints*, arXiv:1509.00469 [5.1, 6]
 Barro, G., Kriek, M., Pérez-González, P. G., et al. 2016, *ApJ*, 827, L32 [1, 3.4, 5.2]
 Belli, S., Newman, A. B., Ellis, R. S., & Konidaris, N. P. 2014, *ApJ*, 788, L29 [5.1]
 Bender, R., Doebereiner, S., & Moellenhoff, C. 1988, *A&AS*, 74, 385 [5.1]
 Bender, R., Surma, P., Doebereiner, S., Moellenhoff, C., & Madejsky, R. 1989, *A&A*, 217, 35 [1]
 Bigiel, F., Leroy, A., Walter, F., et al. 2008, *AJ*, 136, 2846 [6]
 Binney, J., & Tremaine, S. 2008, *Galactic Dynamics: Second Edition* (Princeton University Press) [1]
 Boselli, A., Boissier, S., Cortese, L., et al. 2009, *ApJ*, 706, 1527 [3.1.2]
 Bouché, N., Dekel, A., Genzel, R., et al. 2010, *ApJ*, 718, 1001 [1]
 Brammer, G. B., van Dokkum, P. G., Franx, M., et al. 2012, *ApJS*, 200, 13 [1, 2.1]
 Brinchmann, J., Charlot, S., White, S. D. M., et al. 2004, *MNRAS*, 351, 1151 [1]
 Bruzual, G., & Charlot, S. 2003, *MNRAS*, 344, 1000 [2.1, 1, 3.2, 3.3, A, 11]
 Buat, V., & Xu, C. 1996, *A&A*, 306, 61 [1]
 Buat, V., Iglesias-Páramo, J., Seibert, M., et al. 2005, *ApJ*, 619, L51 [1]
 Caffau, E., Ludwig, H.-G., Steffen, M., Freytag, B., & Bonifacio, P. 2011, *Sol. Phys.*, 268, 255 [13]
 Calzetti, D. 1997, *AJ*, 113, 162 [1]
 Calzetti, D., Armus, L., Bohlin, R. C., et al. 2000, *ApJ*, 533, 682 [1, 2.1, 1, 3.1.2, 3.1.2, 3.2, 3.4, A]
 Calzetti, D., Kinney, A. L., & Storchi-Bergmann, T. 1994, *ApJ*, 429, 582 [1, A]
 Cappellari, M. 2016, *ARA&A*, 54, 597 [1, 5.1]
 Cappellari, M., & Copin, Y. 2003, *MNRAS*, 342, 345 [4.4]
 Cardelli, J. A., Clayton, G. C., & Mathis, J. S. 1989, *ApJ*, 345, 245 [1, 3.1.2]
 Carollo, C. M., Danziger, I. J., & Buson, L. 1993, *MNRAS*, 265, 553 [1, 5.1]
 Carollo, C. M., Bschorr, T. J., Renzini, A., et al. 2013, *ApJ*, 773, 112 [1, 5.1, 6]
 Carollo, C. M., Cibinel, A., Lilly, S. J., et al. 2016, *ApJ*, 818, 180 [5.1]
 Cassata, P., Gialalisco, M., Williams, C. C., et al. 2013, *ApJ*, 775, 106 [1, 5.1]
 Ceverino, D., Klypin, A., Klimek, E. S., et al. 2014, *MNRAS*, 442, 1545 [1, 4.5, 5.2]
 Chabrier, G. 2003, *PASP*, 115, 763 [2.1, 1, 3.1.1, 3.1.2, 3.2, 11]
 Charlot, S., & Fall, S. M. 2000, *ApJ*, 539, 718 [3.4]
 Chevallard, J., Charlot, S., Wandelt, B., & Wild, V. 2013, *MNRAS*, 432, 2061 [3.4]
 Cibinel, A., Carollo, C. M., Lilly, S. J., et al. 2013, *ApJ*, 776, 72 [5.1]
 Civano, F., Marchesi, S., Comastri, A., et al. 2016, *ApJ*, 819, 62 [2.1]
 Cortese, L., Boselli, A., Franzetti, P., et al. 2008, *MNRAS*, 386, 1157 [3.2]
 Daddi, E., Cimatti, A., Renzini, A., et al. 2004, *ApJ*, 617, 746 [4.2]
 Daddi, E., Dickinson, M., Morrison, G., et al. 2007, *ApJ*, 670, 156 [1]
 Daddi, E., Bournaud, F., Walter, F., et al. 2010, *ApJ*, 713, 686 [1]
 Davé, R., Finlator, K., & Oppenheimer, B. D. 2012, *MNRAS*, 421, 98 [1]
 Dayal, P., Ferrara, A., & Dunlop, J. S. 2013, *MNRAS*, 430, 2891 [1]
 Dekel, A., & Burkert, A. 2014, *MNRAS*, 438, 1870 [1]
 Dekel, A., Zolotov, A., Tweed, D., et al. 2013, *MNRAS*, 435, 999 [1]
 Draine, B. T. 2003, *ARA&A*, 41, 241 [1]
 Erb, D. K., Steidel, C. C., Shapley, A. E., et al. 2006, *ApJ*, 647, 128 [3.1.2]
 Faber, S. M., Tremaine, S., Ajhar, E. A., et al. 1997, *AJ*, 114, 1771 [1, 5.1]
 Fagioli, M., Carollo, C. M., Renzini, A., et al. 2016, *ApJ*, 831, 173 [1, 5.1, 6]
 Feldmann, R. 2015, *MNRAS*, 449, 3274 [1]
 Fitzpatrick, E. L. 1999, *PASP*, 111, 63 [1, 3.1.2, 3.4]
 Forrest, B., Tran, K.-V. H., Tomczak, A. R., et al. 2016, *ApJ*, 818, L26 [3.4]
 Förster Schreiber, N. M., Shapley, A. E., Erb, D. K., et al. 2011a, *ApJ*, 731, 65 [2.1]
 Förster Schreiber, N. M., Genzel, R., Bouché, N., et al. 2009, *ApJ*, 706, 1364 [2.1]
 Förster Schreiber, N. M., Shapley, A. E., Genzel, R., et al. 2011b, *ApJ*, 739, 45 [2.1]
 Förster Schreiber, N. M., Genzel, R., Newman, S. F., et al. 2014, *ApJ*, 787, 38 [2.1, 4.2, B]
 Franx, M., van Dokkum, P. G., Schreiber, N. M. F., et al. 2008, *ApJ*, 688, 770 [5.1]

- Genzel, R., Tacconi, L. J., Gracia-Carpio, J., et al. 2010, *MNRAS*, 407, 2091 [1]
- Genzel, R., Tacconi, L. J., Kurk, J., et al. 2013, *ApJ*, 773, 68 [3.4, 4.5]
- Genzel, R., Förster Schreiber, N. M., Rosario, D., et al. 2014a, *ApJ*, 796, 7 [2.1]
- Genzel, R., Förster Schreiber, N. M., Lang, P., et al. 2014b, *ApJ*, 785, 75 [1, 2.1]
- Hayward, C. C., Lanz, L., Ashby, M. L. N., et al. 2014, *MNRAS*, 445, 1598 [4.2]
- Hemmati, S., Mobasher, B., Darvish, B., et al. 2015, *ApJ*, 814, 46 [1, 6]
- Hinshaw, G., Larson, D., Komatsu, E., et al. 2013, *ApJS*, 208, 19 [1]
- Hunter, J. D. 2007, *Computing In Science & Engineering*, 9, 90 [6]
- Ilbert, O., McCracken, H. J., Le Fèvre, O., et al. 2013, *A&A*, 556, A55 [1]
- Kashino, D., Silverman, J. D., Rodighiero, G., et al. 2013, *ApJ*, 777, L8 [3.1.2, 3.1.2]
- Kelson, D. D., & Holden, B. P. 2010, *ApJ*, 713, L28 [4.2]
- Kennicutt, Jr., R. C. 1989, *ApJ*, 344, 685 [6]
- . 1998, *ARA&A*, 36, 189 [3.1.1, 3.1.2, 4.2, 6]
- Kennicutt, Jr., R. C., Hao, C.-N., Calzetti, D., et al. 2009, *ApJ*, 703, 1672 [4.2]
- Koekemoer, A. M., Faber, S. M., Ferguson, H. C., et al. 2011, *ApJS*, 197, 36 [2.3.3]
- Kong, X., Daddi, E., Arimoto, N., et al. 2006, *ApJ*, 638, 72 [2.1]
- Koyama, Y., Kodama, T., Hayashi, M., et al. 2015, *MNRAS*, 453, 879 [3.1.2]
- Kriek, M., & Conroy, C. 2013, *ApJ*, 775, L16 [3.4]
- Krist, J. 1995, in *Astronomical Society of the Pacific Conference Series*, Vol. 77, *Astronomical Data Analysis Software and Systems IV*, ed. R. A. Shaw, H. E. Payne, & J. J. E. Hayes, 349 [2.4]
- Labbé, I., Huang, J., Franx, M., et al. 2005, *ApJ*, 624, L81 [6]
- Leroy, A. K., Bigiel, F., de Blok, W. J. G., et al. 2012, *AJ*, 144, 3 [4.2]
- Lilly, S. J., & Carollo, C. M. 2016, *ApJ*, 833, 1 [1, 5.1, 6]
- Lilly, S. J., Carollo, C. M., Pipino, A., Renzini, A., & Peng, Y. 2013, *ApJ*, 772, 119 [1]
- Lilly, S. J., Le Fèvre, O., Renzini, A., et al. 2007, *ApJS*, 172, 70 [2.1]
- Lilly, S. J., Le Brun, V., Maier, C., et al. 2009, *ApJS*, 184, 218 [2.1]
- Liu, G., Calzetti, D., Hong, S., et al. 2013, *ApJ*, 778, L41 [3.4]
- Lutz, D., Poglitsch, A., Altieri, B., et al. 2011, *A&A*, 532, A90 [4.2]
- Madau, P. 1995, *ApJ*, 441, 18 [A]
- Mancini, C., Förster Schreiber, N. M., Renzini, A., et al. 2011, *ApJ*, 743, 86 [2.1]
- Massey, R., Stoughton, C., Leauthaud, A., et al. 2010, *MNRAS*, 401, 371 [2.3.1]
- Meurer, G. R., Heckman, T. M., & Calzetti, D. 1999, *ApJ*, 521, 64 [1, 3.1.1, A]
- Mosleh, M., Williams, R. J., Franx, M., & Kriek, M. 2011, *ApJ*, 727, 5 [5.1]
- Muñoz-Mateos, J. C., Gil de Paz, A., Boissier, S., et al. 2009, *ApJ*, 701, 1965 [4.4]
- Muzzin, A., van der Burg, R. F. J., McGee, S. L., et al. 2014, *ApJ*, 796, 65 [1]
- Nelson, E. J., van Dokkum, P. G., Momcheva, I. G., et al. 2016a, *ApJ*, 817, L9 [1, 4.4, 6, 6]
- Nelson, E. J., van Dokkum, P. G., Förster Schreiber, N. M., et al. 2016b, *ApJ*, 828, 27 [6]
- Newman, A. B., Ellis, R. S., Bundy, K., & Treu, T. 2012, *ApJ*, 746, 162 [5.1]
- Newman, S. F., Buschkamp, P., Genzel, R., et al. 2014, *ApJ*, 781, 21 [2.1]
- Noeske, K. G., Weiner, B. J., Faber, S. M., et al. 2007, *ApJ*, 660, L43 [1]
- Oesch, P. A., Bouwens, R. J., Carollo, C. M., et al. 2010, *ApJ*, 725, L150 [5.1]
- Panuzzo, P., Bressan, A., Granato, G. L., Silva, L., & Danese, L. 2003, *A&A*, 409, 99 [1]
- Peng, Y.-j., Lilly, S. J., Kovač, K., et al. 2010, *ApJ*, 721, 193 [1]
- Penner, K., Dickinson, M., Weiner, B., et al. 2015, *ArXiv e-prints*, arXiv:1507.00728 [3.4]
- Poggianti, B. M., Calvi, R., Bindoni, D., et al. 2013, *ApJ*, 762, 77 [1]
- Price, S. H., Kriek, M., Brammer, G. B., et al. 2014, *ApJ*, 788, 86 [3.1.2]
- Puglisi, A., Rodighiero, G., Franceschini, A., et al. 2016, *A&A*, 586, A83 [3.1.2]
- Rafelski, M., Teplitz, H. I., Gardner, J. P., et al. 2015, *AJ*, 150, 31 [2.3.2, 2.4, 6]
- Reddy, N. A., Erb, D. K., Pettini, M., Steidel, C. C., & Shapley, A. E. 2010, *ApJ*, 712, 1070 [3.1.2]
- Reddy, N. A., Kriek, M., Shapley, A. E., et al. 2015, *ApJ*, 806, 259 [1, 3.4]
- Renzini, A. 2016, *MNRAS*, 460, L45 [6]
- Rhodes, J., Leauthaud, A., Stoughton, C., et al. 2010, *PASP*, 122, 439 [2.3.1]
- Rix, H.-W., Carollo, C. M., & Freeman, K. 1999, *ApJ*, 513, L25 [5.1]
- Rodighiero, G., Daddi, E., Baronchelli, I., et al. 2011, *ApJ*, 739, L40 [1]
- Rodighiero, G., Renzini, A., Daddi, E., et al. 2014, *MNRAS*, 443, 19 [1, 5.1]
- Salim, S., Rich, R. M., Charlot, S., et al. 2007, *ApJS*, 173, 267 [1]
- Salim, S., Dickinson, M., Michael Rich, R., et al. 2009, *ApJ*, 700, 161 [4.2]
- Salmon, B., Papovich, C., Long, J., et al. 2016, *ApJ*, 827, 20 [3.4]
- Salpeter, E. E. 1955, *ApJ*, 121, 161 [3.2]
- Saracco, P., Gargiulo, A., & Longhetti, M. 2012, *MNRAS*, 422, 3107 [1, 6]
- Saracco, P., Longhetti, M., & Gargiulo, A. 2011, *MNRAS*, 412, 2707 [1]
- Sauvage, M., & Thuan, T. X. 1992, *ApJ*, 396, L69 [4.2]
- Schinnerer, E., Sargent, M. T., Bondi, M., et al. 2010, *ApJS*, 188, 384 [4.2]
- Schmidt, M. 1959, *ApJ*, 129, 243 [6]
- Schreiber, C., Pannella, M., Elbaz, D., et al. 2015, *A&A*, 575, A74 [1, 5.1, 5.2]
- Seaton, M. J. 1979, *MNRAS*, 187, 73P [1]
- Sérsic, J. L. 1968, *Atlas de galaxies australes* (Cordoba, Argentina: Observatorio Astronomico) [4.4]
- Shen, S., Mo, H. J., White, S. D. M., et al. 2003, *MNRAS*, 343, 978 [5.1]
- Silverman, J. D., Daddi, E., Rodighiero, G., et al. 2015, *ApJ*, 812, L23 [5.2]
- Skelton, R. E., Whitaker, K. E., Momcheva, I. G., et al. 2014, *ApJS*, 214, 24 [2.1]
- Smith, B. J., Harvey, P. M., Colome, C., et al. 1994, *ApJ*, 425, 91 [4.2]
- Somerville, R. S., Behroozi, P., Pandya, V., et al. 2017, *ArXiv e-prints*, arXiv:1701.03526 [5.1]
- Speagle, J. S., Steinhardt, C. L., Capak, P. L., & Silverman, J. D. 2014, *ApJS*, 214, 15 [1]
- Steidel, C. C., Shapley, A. E., Pettini, M., et al. 2004, *ApJ*, 604, 534 [2.1]
- Tacchella, S., Dekel, A., Carollo, C. M., et al. 2016a, *MNRAS*, 458, 242 [1, 4.5, 5.2, 6]
- . 2016b, *MNRAS*, 457, 2790 [1, 10, 5.2, 6]
- Tacchella, S., Carollo, C. M., Renzini, A., et al. 2015a, *Science*, 348, 314 [1, 2.1, 4.4, 4.5, 4.6, 5.1, 5.2, 6]
- Tacchella, S., Lang, P., Carollo, C. M., et al. 2015b, *ApJ*, 802, 101 [2.1, 2.3.3, 2.4, 4.4]
- Tacconi, L. J., Genzel, R., Neri, R., et al. 2010, *Nature*, 463, 781 [1]
- Tadaki, K.-i., Kohno, K., Kodama, T., et al. 2015, *ApJ*, 811, L3 [1, 3.4]
- Tadaki, K.-i., Genzel, R., Kodama, T., et al. 2017, *ApJ*, 834, 135 [1, 3.4, 5.2]
- Teplitz, H. I., Rafelski, M., Kurczynski, P., et al. 2013, *AJ*, 146, 159 [2.3.2]
- Utomo, D., Kriek, M., Labbé, I., Conroy, C., & Fumagalli, M. 2014, *ApJ*, 783, L30 [4.2]
- Valentino, F., Daddi, E., Strazzullo, V., et al. 2015, *ApJ*, 801, 132 [3.1.2]
- Valentinuzzi, T., Fritz, J., Poggianti, B. M., et al. 2010, *ApJ*, 712, 226 [1]

- van Dokkum, P. G., Franx, M., Kriek, M., et al. 2008, ApJ, 677, L5 [5.1]
 van Dokkum, P. G., Whitaker, K. E., Brammer, G., et al. 2010, ApJ, 709, 1018 [1]
 van Dokkum, P. G., Bezanson, R., van der Wel, A., et al. 2014, ApJ, 791, 45 [1]
 Whitaker, K. E., van Dokkum, P. G., Brammer, G., & Franx, M. 2012, ApJ, 754, L29 [1]
 Whitaker, K. E., Franx, M., Leja, J., et al. 2014, ApJ, 795, 104 [1, 2.1, 2, 5.1, 5.2]
 Wilkins, S. M., Bunker, A. J., Stanway, E., Lorenzoni, S., & Caruana, J. 2011, MNRAS, 417, 717 [3.2]
 Williams, C. C., Giavalisco, M., Bezanson, R., et al. 2016, ArXiv e-prints, arXiv:1607.06089 [1]
 Williams, R. J., Quadri, R. F., Franx, M., van Dokkum, P., & Labbé, I. 2009, ApJ, 691, 1879 [6]

- Witt, A. N., & Gordon, K. D. 2000, ApJ, 528, 799 [1, 3.4]
 Wuyts, S., Labbé, I., Franx, M., et al. 2007, ApJ, 655, 51 [6]
 Wuyts, S., Förster Schreiber, N. M., van der Wel, A., et al. 2011, ApJ, 742, 96 [3.4, 4.2]
 Wuyts, S., Förster Schreiber, N. M., Genzel, R., et al. 2012, ApJ, 753, 114 [1, 4.4, 6]
 Wuyts, S., Förster Schreiber, N. M., Nelson, E. J., et al. 2013, ApJ, 779, 135 [3.1.2, 3.1.2, 4.4]
 Zeimann, G. R., Ciardullo, R., Gronwall, C., et al. 2015, ApJ, 814, 162 [3.4]
 Zolotov, A., Dekel, A., Mandelker, N., et al. 2015, MNRAS, 450, 2327 [1, 4.5, 5.2]

APPENDIX

A. DUST ATTENUATION PARAMETERS FROM (FUV–NUV) COLOR

We derive the (FUV–NUV)– A_V and (FUV–NUV)– β conversions in Figure 11 by generating a set of model SEDs from Bruzual & Charlot (2003), for six different metallicities ($Z=0.0001, 0.0004, 0.004, 0.008, 0.02$, and 0.05) and three different star-formation histories (SFHs; constant, exponentially rising, and exponentially decreasing). The timescales used for the rising and declining SFHs are respectively $\tau = [-5000, -1000, -500, -50, 50, 250, 500, 1000, 5000, 10000]$ Myr. Note the negative sign indicates rising SFHs. The stellar age is defined as the age since the onset of star formation. We consider a minimum age of 10 Myr and a maximum age of 3.5 Gyr (age of the universe at $z \sim 2$). We assume that the dust attenuation is described by the Calzetti dust attenuation curve (Calzetti et al. 2000), with A_V varying from 0.0 to 6.0, in steps of 0.05 between 0.0 and 4.0, in steps of 0.25 between 4.0 and 5, and in steps of 0.5 between 5.0 and 6.0. The intergalactic medium (IGM) is treated using the Madau (1995) prescription. Redshifts vary between 2.0 and 2.5 in steps of 0.1.

As shown in the top panel of Figure 11, at a fixed redshift we find a tight correlation between the observed $B_{428} - I_{814}$ color (approximately corresponding to the rest frame FUV–NUV color) and A_V , with a small but significant dependence on redshift (see center and bottom panels). These correlations are well approximated with

$$A_V = (2.36 \pm 0.11) + (2.11 \pm 0.01) \times (B - I)_{z_{\text{obs}}} - (4.11 \pm 0.40) \times \log(1 + z_{\text{obs}}) - (1.78 \pm 0.05) \times \log(1 + z_{\text{obs}}) \times (B - I)_{z_{\text{obs}}}, \quad (\text{A1})$$

where $(B - I)_{z_{\text{obs}}}$ is the observed $(B - I)$ color in mag and z_{obs} is the redshift of the observed galaxy.

For $z_{\text{obs}} = 2.2$, we get:

$$A_V = (0.28 \pm 0.41) + (0.77 \pm 0.05) \times (B - I)_{z_{\text{obs}}=2.2} \quad (\text{A2})$$

similar to the expression suggested by Meurer et al. (1999).

For each model SED, we calculated the UV slope (β) by fitting the flux of the SED model as a function of wavelength, using only those flux points that lie within

the 10 continuum windows given in Calzetti et al. (1994). The typical formal uncertainty in β , when using the 10 aforementioned windows, is $\Delta\beta \approx 0.1$.

We find a tight correlation between the (FUV–NUV) color and β , similar to above:

$$\beta = (0.41 \pm 0.08) + (2.28 \pm 0.01) \times (B - I)_{z_{\text{obs}}} - (5.03 \pm 0.30) \times \log(1 + z_{\text{obs}}) - (1.86 \pm 0.04) \times \log(1 + z_{\text{obs}}) \times (B - I)_{z_{\text{obs}}}. \quad (\text{A3})$$

For $z_{\text{obs}} = 2.2$, we get:

$$\beta = (-2.13 \pm 0.31) + (1.34 \pm 0.04) \times (B - I)_{z_{\text{obs}}=2.2}. \quad (\text{A4})$$

B. RELIABILITY OF SFR FROM IR

As mentioned in Section 4.2, there is the danger of source confusion when using the IR to estimate the SFR. To minimize this problem at the longest wavelengths (i.e. $\lambda \gtrsim 100 \mu\text{m}$), the $24 \mu\text{m}$ source detections are used as priors. We check in this section the reliability of the $\text{SFR}_{\text{IR+UV}}$ for ZC400528 and ZC407306, since both of these galaxies have $\text{SFR}_{\text{IR+UV}}$ values that are significantly larger than dust-corrected SFR_{UV} values.

In Figures 12 and 13 we compare the *Spitzer* MIPS $24 \mu\text{m}$ with the *HST* WFC3 *H*-band images for ZC400528 and ZC407302, respectively. ZC407302 has a bright, low- z neighbor that boosts the IR flux and therefore makes the IR photometry of this galaxy unreliable. Hence, throughout the paper, we have used as the fiducial SFR the dust-corrected UV SFR estimate. ZC400528 has also a neighboring galaxy, though this counterpart is much fainter. In addition, ZC400528 shows a nuclear outflow (Förster Schreiber et al. 2014) and the 1.4 GHz VLA radio data implies a $\text{SFR} \approx 790 M_{\odot} \text{ yr}^{-1}$, both pointing to AGN activity. However, it is unclear how much an AGN could contribute to the IR and radio measurements. Therefore, for this galaxy, we use as the fiducial SFR the UV+IR SFR estimate, though further followups are needed, f.e., with spatially resolved dust continuum measurements.

C. $\text{SFR}_{\text{IR+UV}}$ VERSUS DUST-CORRECTED SFR_{UV}

In addition to the discussion of the SFR from the IR and UV in Section 4.2 (and Figure 4 we show in Figure 14 the SFR estimated from the dust-corrected UV SFR map versus the SFR estimated from the integrated UV+IR photometry. For Q2343-BX610 and Q2346-BX482, no IR data is available, while for ZC407302 the IR photom-

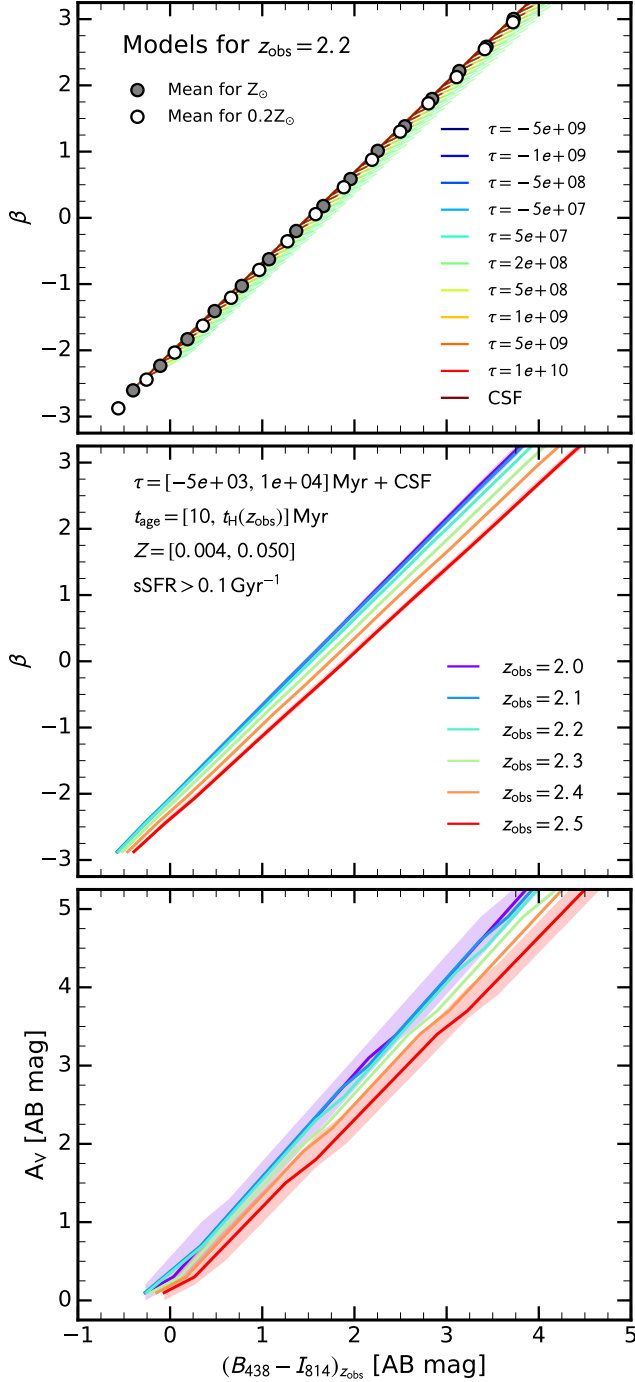


Figure 11. Relations between dust attenuation (UV continuum slope β and total attenuation at V A_V) and observed color $B_{428} - I_{814}$ (rest-frame FUV-NUV). Top panel: relation between β and $B_{428} - I_{814}$ for a large grid of different SED-models at a fixed redshift $z_{\text{obs}} = 2.2$ and for a star-forming population ($\text{sSFR} > 0.1 \text{ Gyr}^{-1}$). The various curves plotted in colors are computed from Bruzual & Charlot (2003) models with solar metallicity and a Chabrier (2003) IMF. Different colors are used for different star formation histories: a suite of exponentially declining and increasing SFRs with different e -folding timescales, and constant SFR. Age increases along each model curve from blue to red $B_{428} - I_{814}$ colors and low to high β . The gray-filled and white-filled circles show the mean relationship derived from solar and $1/5$ solar metallicity models. Middle and bottom panels: mean dependence of β and A_V on $B_{428} - I_{814}$ at different redshifts ($z_{\text{obs}} = 2.0 - 2.5$). Overall, the relations between dust attenuation and the observed $B_{428} - I_{814}$ are tight and have a weak redshift dependence. Therefore, we use the $B_{428} - I_{814}$ to estimate the dust attenuation as given in Equations A3 and A1 (best-fitting relations).

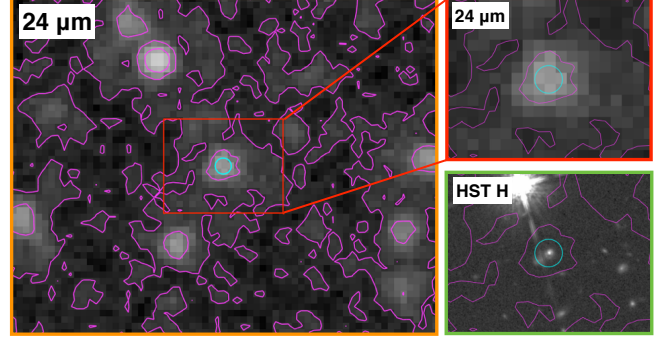


Figure 12. Comparison of the *Spitzer* MIPS $24 \mu\text{m}$ image with the *HST* WFC3 *H*-band image for galaxy ZC400528. North is up in all panels. The left panel shows a $1.3' \times 1.0'$ cutout of the $24 \mu\text{m}$ image. The upper right panel shows zoom-in (approximately $0.4' \times 0.3'$) on the $24 \mu\text{m}$ image, which is marked with a red box in the left panel. The lower right panel shows the same region of the *HST* *H*-band image. In all panels, the magenta lines indicate the contours of the $24 \mu\text{m}$ flux map and the cyan circle shows an aperture of $3''$, centered on ZC400528. There is a close (projected distance is about $1.''54 \approx 13 \text{ kpc}$) neighbor in the South-Eastern region of ZC400528 which contributes to the $24 \mu\text{m}$ and therefore also to the $100 \mu\text{m}$ flux, making the $\text{SFR}_{100\mu\text{m}+\text{UV}}$ difficult to interpret.

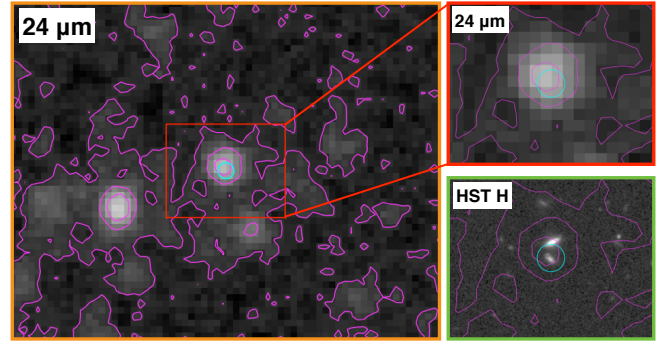


Figure 13. Same as Figure 12, but for galaxy ZC407302. The $24 \mu\text{m}$ -detection clearly encompasses ZC407302 and the Northern, low- z counterpart seen in the *HST* image, which contaminates the $24 \mu\text{m}$ flux and therefore the $\text{SFR}_{24\mu\text{m}+\text{UV}}$ unreliable.

etry is not reliable, as highlighted above (see Figure 13). Three galaxies (ZC405226, ZC405501, ZC412369) are not detected in the IR, i.e., we have upper limits that are consistent with the SFR estimated from the dust-corrected UV SFR map. Four galaxies are detected in the IR: for three objects (D3A15504, ZC400569, ZC406690) both SFR estimates agree well, while for ZC400528 the $\text{SFR}_{\text{IR}+\text{UV}}$ is about 1 dex higher than the SFR from the UV map. However, as highlighted above, this galaxy has a neighbor and also shows some AGN activity. Hence, the IR flux should be interpreted with care and further investigation is needed in the future. Overall, we find good agreement between these two estimates, which indicates that there is no evidence for substantial more star formation hidden by dust relative to what we infer from our dust-corrected, resolved UV SFRs.

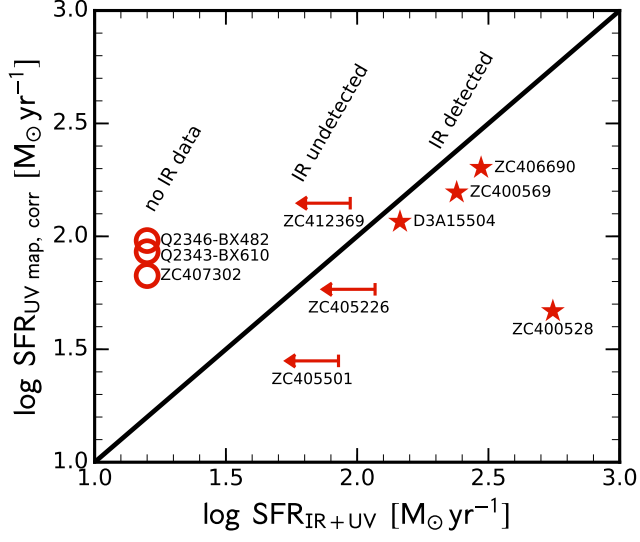


Figure 14. Comparison of the SFR estimated from the dust-corrected UV-SFR map and the integrated UV+IR photometry. Both SFR estimates agree for three of our four IR detected objects (D3A15504, ZC400569, ZC406690), while for ZC400528 the UV+IR SFR estimate is significantly higher. For three objects (ZC405226, ZC405501, ZC412369) we have IR upper limit, which are consistent with the SFR estimate from the dust-corrected UV-SFR map. For two galaxies (Q2343-BX610 and Q2346-BX482) no IR data is available, while for ZC407302 the IR photometry is not reliable because of a bright neighbor, see Figure 13.